Journal of The Electrochemical Society, 2020 **167** 100515

Prediction of Reversible Lithium Plating with a Pseudo-3D Lithium-Ion Battery Model

Serena Carelli[z] **and Wolfgang G. Bessler**[*]

Institute of Energy Systems Technology (INES), Offenburg University of Applied Sciences, 77652 Offenburg, Germany

Fast charging of lithium-ion batteries remains one of the most delicate challenges for the automotive industry, being seriously affected by the formation of lithium metal in the negative electrode. Here we present a physicochemical pseudo-3D model that explicitly includes the plating reaction as side reaction running in parallel to the main intercalation reaction. The thermodynamics of the plating reaction are modeled depending on temperature and ion concentration, which differs from the often-used assumption of a constant plating condition of 0 V anode potential. The reaction kinetics are described with an Arrhenius-type rate law parameterized from an extensive literature research. Re-intercalation of plated lithium was modeled to take place either via reverse plating (solution-mediated) or via an explicit interfacial reaction (surface-mediated). At low temperatures not only the main processes (intercalation and solid-state diffusion) become slow, but also the plating reaction itself becomes slower. Using this model, we are able to predict typical macroscopic experimental observables that are indicative of plating, that is, a voltage plateau during discharge and a voltage drop upon temperature increase. A spatiotemporal analysis of the internal cell states allows a quantitative insight into the competition between intercalation and plating. Finally, we calculate operation maps over a wide range of C-rates and temperatures that allow to assess plating propensity as function of operating condition.
 [DOI: 10.1149/1945-7111/ab95c8]

Manuscript submitted December 19, 2019; revised manuscript received May 13, 2020. Published June 4, 2020.

The efficient and fast charging of lithium-ion batteries remains one of the key challenges for the automotive and energy industries, being seriously affected by the formation of metallic lithium on the surface of the negative electrode.[1] This degradation process, also referred to as lithium plating, damages the mechanical and chemical integrity of the electrode and, as a result, causes capacity loss and internal-resistance increase.[2] Under certain conditions, the formation of a metallic lithium phase at the interface between the anode and the electrolyte competes with and even replaces the intercalation process. In case of cumulative plating, dendrites could form and eventually pierce the separator, creating an electrical short circuit and a consequent fire hazard.[3,4]

It is very difficult to detect lithium plating in situ without a direct observation of the open electrode via microscopy techniques, but it is possible to deduce its presence by analyzing the cell voltage behavior during charge/discharge cycles under plating conditions. Some peculiarities in the cell behavior have been shown to indicate the presence of plated lithium: the most common ones are a *voltage plateau* due to lithium oxidation during discharge at constant temperature[5–14] and a *voltage drop* due to re-intercalation of metallic lithium during heating of the cell.[14–18] On the other hand, the absence of any obvious changes in voltage should not be considered as evidence of a complete absence of lithium plating.[1,14,19] Inhomogeneity in the cell could smear indeed the plateau up to extinction and, in case of a fast-chemical intercalation, accelerated side reactions or a high degree of plating irreversibility, the quantity of plated lithium available for stripping could be under the limits of detection.

Modeling and simulation offer a detailed insight into internal states of battery cells and therefore allow a knowledge-based interpretation of complex macroscopic behavior.[20] A relatively simple way to assess plating risk with pseudo-two-dimensional (P2D) "Newman-type" models has been to compare the simulated local anode potential $\Delta\Phi_{an}$ with the thermodynamic plating condition of $\Delta\Phi_{Li}^{eq} = 0$ V.[21–27] This approach has several pitfalls that have not been well discussed in literature. Firstly, it has to be ensured that the graphite half-cell potential ($\Delta\Phi_{LiC6}^{eq}$ as function of intercalated lithium stoichiometry) used as model input has the correct potential reference of 0 V vs Li/Li$^+$. The half-cell potential is usually represented in tabular or analytical form as obtained from "half-cell measurements." In order to ensure the 0 V reference, these measurements should use lithium metal as reference electrode. Secondly, the thermodynamics of the plating reaction depend on temperature, pressure and lithium ion concentration. This means that $\Delta\Phi_{Li}^{eq}$ is not constant equal to zero, as usually assumed, but depends on operating conditions. This will be discussed in detail in this paper and included in the present model. Thirdly, using a thermodynamic plating condition ignores the kinetics of the plating reaction. Anode potentials $\Delta\Phi_{an} < \Delta\Phi_{Li}^{eq}$ do not necessarily induce plating if it is kinetically hindered. At low temperatures, which are usually seen to support plating, not only the main processes (intercalation and solid-state diffusion) become slow, but also the plating reaction itself becomes slow. This effect will also be included in the present model.

This article presents the extension of a previously developed[28] pseudo-three-dimensional (P3D) model of a commercial 350 mAh high-power lithium-ion pouch cell with the purpose of simulating reversible lithium plating over a wide range of operating conditions. The plating reaction is implemented as reversible reaction, and no irreversible processes such as SEI formation or detachment of plated lithium from the particle surface are considered at the present stage. An extensive literature research was carried out in order to identify accurate rate coefficients for the plating reaction. Experimental verification was possible by comparison with experiments on our reference cell,[28] in which no plating hints were apparent, and with the work of Ecker[14] on a similar (but not identical) cell in which the above-mentioned plating hints (*voltage plateau* and *voltage drop*) are clearly visible. This work introduces the following original features: (i) Explicit inclusion of the lithium plating reaction at the anode, including a continuity equation for metallic lithium; (ii) verification by comparison with experiments showing *voltage plateau* and *voltage drop* as plating indicators; (iii) inclusion of a reversible re-intercalation reaction in the specific case of a cell not showing evident plating signs; (iv) spatiotemporal analysis at the internal cell states for a detailed insight on the plating mechanism; and (v) calculation of operation maps over a wide range of C-rates and temperatures.

In the following Section, fundamental thermodynamic and kinetic aspects of the plating reaction are discussed. Then the modeling methodology is presented, followed by a comparison between simulations and experiments and further plating simulations. Finally, the findings are concluded in the Summary.

Thermodynamics and Kinetics of Lithium Plating

Plating thermodynamics.—Globally, plating can be described as single-electron charge-transfer reaction according to

*Electrochemical Society Member.
[z]E-mail: serena.carelli@hs-offenburg.de

$$\mathrm{Li^+[elyt]} + \mathrm{e^-[elde]} \rightleftharpoons \mathrm{Li[metal]}, \quad [1]$$

where, Li[metal] represents plated lithium and elyt and elde stand for electrolyte and electrode, respectively. We formulate this reaction in reduction direction, as common in electrochemistry.[29] Equation 1 is a global reaction; although microkinetically it may consist of a combination of multiple consecutive or parallel elementary reaction steps, the global equation is sufficient to discuss the thermodynamics. The equilibrium potential of this reaction, $\Delta\Phi_{\mathrm{Li}}^{\mathrm{eq}}$, is often assigned a canonical value of 0 V vs Li/Li$^+$,[30–32] which is somewhat trivial. It is, however, important to note that $\Delta\Phi_{\mathrm{Li}}^{\mathrm{eq}}$ is not constant, but depends on temperature, pressure, and concentration of all involved species. This means that $\Delta\Phi_{\mathrm{Li}}^{\mathrm{eq}}$ varies also with the operational conditions, that is, cell current (affecting local Li$^+$ concentration) and operation temperature. In order to reliably predict plating, it is necessary to include these dependencies in the analysis.

Quantitatively, the concentration dependence of $\Delta\Phi_{\mathrm{Li}}^{\mathrm{eq}}$ is described by the Nernst equation,

$$\Delta\Phi_{\mathrm{Li}}^{\mathrm{eq}} = -\frac{\Delta G^0(p,T)}{zF} - \frac{RT}{zF}\cdot \ln\left(\prod_{i=1}^{N_{\mathrm{R}},N_{\mathrm{P}}}\left(\frac{c_i}{c_i^0}\right)^{\nu_i}\right), \quad [2]$$

where, $\Delta G^0(p,T)$ is the standard Gibbs energy of reaction, which is a function of pressure and temperature, but not of concentration; in fact, it is defined for standard concentrations c_i^0 (note the concentration-dependent term of Eq. 2 vanishes for $c_i = c_i^0$). Note a list of symbols is given in the Appendix. In formulating Eq. 2 as function of concentrations, we assume that activity is equal to concentration (activity coefficient of unity for all species). For Li$^+$[elyt], this is likely a simplifying assumption; from transport experiments, it is well-known that the concentrated electrolytes used in lithium-ion batteries behave non-ideally.[33] It is beyond the scope of the present work to measure or predict activity coefficients. For Li[metal], we believe that the assumption is valid; note that in the numerical simulations shown further below, activity is set to zero if the solid phase vanishes. In the following, we neglect the pressure dependence of ΔG^0 and assume atmospheric pressure. The Gibbs energy of reaction can be obtained from the standard-state chemical potentials μ_i^0 of all species i involved in reaction (1) according to

$$\Delta G^0(T) = \sum_{i=1}^{N_{\mathrm{R}},N_{\mathrm{P}}} \nu_i \mu_i^0(T), \quad [3]$$

and the standard-state chemical potentials can be calculated from the molar enthalpies, $h_i^0(T)$, and molar entropies, $s_i^0(T)$, according to

$$\mu_i^0(T) = h_i^0(T) - Ts_i^0(T). \quad [4]$$

For applying these equations to the plating reaction (1), molar thermodynamic parameters are needed for the involved species Li[metal], Li$^+$[elyt], and e$^-$[elde]. Molar enthalpies, entropies and heat capacities as function of temperature have been compiled for a large number of compounds in the NASA thermochemical tables.[34] The tables provide polynomial functions according to

$$\frac{h^0(T)}{RT} = a_1 + a_2\frac{(T/\mathrm{K})}{2} + a_3\frac{(T/\mathrm{K})^2}{3} + a_4\frac{(T/\mathrm{K})^3}{4} + a_5\frac{(T/\mathrm{K})^4}{5} + \frac{b_1}{(T/\mathrm{K})}, \quad [5]$$

$$\frac{s^0(T)}{R} = a_1\ln(T/\mathrm{K}) + a_2(T/\mathrm{K}) + a_3\frac{(T/\mathrm{K})^2}{2} + a_4\frac{(T/\mathrm{K})^3}{3} + a_5\frac{(T/\mathrm{K})^4}{4} + b_2, \quad [6]$$

$$\frac{c_p^0(T)}{R} = a_1 + a_2(T/\mathrm{K}) + a_3(T/\mathrm{K})^2 + a_4(T/\mathrm{K})^3 + a_5(T/\mathrm{K})^4. \quad [7]$$

where, $T^0 = 298.15$ K is the standard temperature and $c_{p,i}^0$ the molar heat capacity. For crystalline metallic lithium Li[metal][35], $a_1 = 6.10909942\cdot10^{-1}$, $a_2 = 1.41041217\cdot10^{-2}$, $a_3 = -1.74958170\cdot10^{-5}$, $a_4 = -3.33741023\cdot10^{-8}$, $a_5 = 7.76629665\cdot10^{-11}$, $b_1 = -6.25121208\cdot10^{2}$, $b_2 = -3.26449947\cdot10^{0}$. At a standard temperature of 298.15 K, these equations yield values of $h_{\mathrm{Li[metal]}}^0 = 0$ (thermodynamic reference for pure elements), $s_{\mathrm{Li[metal]}}^0 = 29.12\frac{\mathrm{J}}{\mathrm{K\cdot mol}}$, and $c_{p,\mathrm{Li[metal]}}^0 = 24.86\frac{\mathrm{J}}{\mathrm{K\cdot mol}}$. Note that these values are given for crystalline lithium. The thermodynamic properties of plated lithium on graphite particles inside a LIB electrode are likely different. It is out of scope of the present work to validate the used data, or to measure or predict these properties. However, within the present modeling framework, it would be straightforward to insert alternative parameters when available.

The molar thermodynamic properties of dissolved lithium ions in lithium-ion battery electrolytes, Li$^+$[elyt], are unavailable in literature. In fact, absolute thermodynamic values for dissolved ions are not easily accessible and are subject of controversy even for the most simple system, that is, protons in aqueous solution.[36,37] Fortunately, only relative values needed, and a thermodynamic reference can be defined arbitrarily. Here we assume Li$^+$[elyt] as reference species and therefore assign $h_{\mathrm{Li^+[elyt]}}^0 = 0$ and $s_{\mathrm{Li^+[elyt]}}^0 = 0$. This assumption will not influence the present results, because the values affect both intercalation and plating reactions in the same way. They would become important if other ions enter the reaction system (which is not the case for the plating and intercalation reactions) or if different solvent systems are compared (which is not the case in the present study). Note that a standard entropy of zero is also used in aqueous electrochemistry as reference ($s_{\mathrm{H^+[H_2O]}}^0 = 0$),[38] therefore it is reasonable, unless other data become available, to use a similar reference for lithium-ion battery electrolytes. The same reasoning applies to electrons, therefore we assign $h_{\mathrm{e^-[elde]}}^0 = 0$ and $s_{\mathrm{e^-[elde]}}^0 = 0$.

Using these parameters, Eqs. 2–7 allow to calculate $\Delta\Phi_{\mathrm{Li}}^{\mathrm{eq}}$ as function of temperature and lithium-ion concentration. Results are shown in Fig. 1a for concentrations $c_{\mathrm{Li^+[elyt]}}$ from 0.5 to 2 M and temperatures from −20 to 30 °C. In this colormap the values are plotted relative to the $\Delta\Phi_{\mathrm{Li}}^{\mathrm{eq}}$ value at 25°C and a Li$^+$ concentration of 1 M, which we assume as reference conditions for $\Delta\Phi_{\mathrm{Li}}^{\mathrm{eq}} = 0$. As shown here, the $\Delta\Phi_{\mathrm{Li}}^{\mathrm{eq}}$ is not constant at 0 V as often simplistically described in literature, but varies according to the operational conditions. In particular, for concentrations between 0.5 and 2 M it varies by 28 mV at −20 °C and by 34 mV at 30 °C, where higher concentrations increase the equilibrium plating potential. From the Nernst Eq. 2, a linear increase of $\Delta\Phi_{\mathrm{Li}}^{\mathrm{eq}}$ with $\ln c_{\mathrm{Li^+}}$ with a slope of RT/F is expected. This behavior has also been shown experimentally using a concentration cell, where a linear behavior of $\Delta\Phi_{\mathrm{Li}}^{\mathrm{eq}}$ vs $\ln c_{\mathrm{Li^+}}$ was observed for concentrations $\leqslant 1$ mol l^{-1}.[39] Surprisingly smaller is the influence of temperature, with no difference at 0.5 M for temperatures between −20 and 30 °C and the spread increasing to a maximum of only 5.2 mV at 2 M, where higher temperatures again increase the equilibrium plating potential.

Although the results show that the plating thermodynamics significantly depend on operating conditions, the interplay between plating and intercalation is of high importance. We therefore need to extend the analysis to the intercalation reaction at the graphite active material, which is formulated as

$$\mathrm{Li^+[elyt]} + \mathrm{e^-[elde]} + \mathrm{V[C_6]} \rightleftharpoons \mathrm{Li[C_6]}. \quad [8]$$

Here, Li[C$_6$] represents intercalated lithium and V[C$_6$] represents vacancies, both including the host matrix. Similar to plating, the

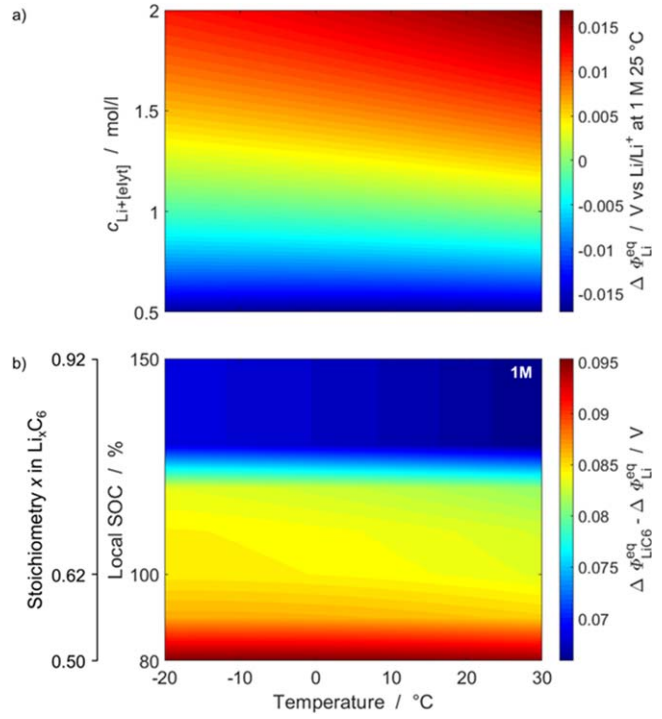

Figure 1. (a) Equilibrium potential $\Delta\Phi_{Li}^{eq}$ for $c_{Li^+[elyt]}$ from 0.5 to 2 M and temperatures from −20 to 30 °C. The values are plotted relative to the value at 25 °C and 1 M (reference conditions for $\Delta\Phi_{Li}^{eq} = 0$). (b) Equilibrium potential difference $\Delta(\Delta\Phi) = \Delta\Phi_{LiC6}^{eq} - \Delta\Phi_{Li}^{eq}$ for temperatures varying from −20 to 30 °C and SOC from 80 to 150%.

thermodynamics of the intercalation reaction also depends on lithium ion concentration and on temperature, but has an additional strong dependence on intercalated lithium stoichiometry. Hence, we need additional molar thermodynamic parameters for intercalated lithium, $Li[C_6]$, and vacancies, $V[C_6]$, as function of lithium stoichiometry. The modeling and parameterization of $h_{Li[C_6]}^0$, $s_{Li[C_6]}^0$, $h_{V[C_6]}^0$ and $s_{V[C_6]}^0$ was described in detail in Ref. 40, and parameters are given in Refs. 28, 41 Briefly, published half-cell experiments (voltage as function of lithium stoichiometry using lithium metal as counter electrode) were used to derive molar enthalpies and entropies of the intercalation compound. In this process, the same thermodynamic data of Li[metal] as presented above and used here were used to subtract out the influence of the lithium counter electrode.[40] Therefore, the Li[metal] and $Li[C_6]$ data are self-consistent, which is of course a requirement for correctly predicting plating onset.

As plating and intercalation compete for electrons and lithium ions (cf. Eqs. 1 and 8), we will discuss the equilibrium potential difference $\Delta(\Delta\Phi) = \Delta\Phi_{LiC6}^{eq} - \Delta\Phi_{Li}^{eq}$ as indicator of the thermodynamic driving force of plating vs intercalation. Fig. 1b) shows $\Delta(\Delta\Phi)$ as function of temperature varying from −20 to 30 °C and as function of state of charge (SOC) of the graphite from 80 to 150% (and relative stoichiometry, where $X_{Li[C6]} = 0.619$ corresponds to the stoichiometry of a fully-charged battery[28]). SOC values over 100% show $\Delta(\Delta\Phi)$ during overlithiation, which is one of the conditions in which lithium plating is expected to be found. It can be seen that $\Delta(\Delta\Phi)$ has positive values throughout, in fact varying between approx. 65 and 95 mV within the investigated parameter ranges (84 mV at SOC 100%). This means that, under equilibrium, intercalation is always favored over plating. $\Delta(\Delta\Phi)$ depends mainly on SOC and shows only a small dependence on temperature. It should be noted that, although the data shown in Fig. 1b) were calculated for $c_{Li^+[elyt]} = 1$ M, they are independent of the lithium ion concentration, because $c_{Li^+[elyt]}$ affects the thermodynamics of both reactions in the same way.[39,42]

From this discussion it can be concluded that not only thermodynamics, but also kinetics has a dominant influence on plating, and in particular on its temperature and C-rate (hence concentration) dependence.

Plating kinetics.—Kinetics play a key role in battery chemistry, both for the intercalation main reaction and the plating side reaction. Both reactions are thermally-activated (reaction rates decrease with decreasing temperature), potential-driven (reaction rates increase with decreasing potential), and concentration-influenced (reaction rates depend on $Li^+[elyt]$ and $Li[C_6]$ concentrations). In the cell (and in the present model), both reactions take place in parallel and compete for electrons and lithium ions. The relative kinetics of both reactions therefore dominantly govern the plating risk.

We model the kinetics of (electro)chemical reactions based on transition state theory,[29,33] which can be algebraically manipulated[43] to obtain the Butler–Volmer form

$$i = i^0\left[\exp\left(\frac{\alpha_c zF}{RT}\eta_{act}\right) - \exp\left(-\frac{(1-\alpha_c)zF}{RT}\eta_{act}\right)\right] \qquad [9]$$

with the exchange current density

$$i^0 = i^{00}\exp\left(-\frac{E_{act}}{RT}\right)\cdot\prod_{i=1}^{N_R}\left(\frac{c_i}{c_i^0}\right)^{(1-\alpha_c)}\prod_{i=1}^{N_P}\left(\frac{c_i}{c_i^0}\right)^{\alpha_c}, \qquad [10]$$

where, i^{00} is assumed constant. This form is used for both the intercalation reaction (8) and the plating reaction (1). Similar as for the Nernst equation (Eq. 2), this formulation is based on the simplifying assumption that activities are equal to concentrations (unity activity coefficients).

An accurate parameterization of the mass-action kinetics parameters i^{00}, E_{act} and α_c of both reactions is required in order to simulate the competition mechanism. While we take the kinetic parameters of the intercalation reaction from our previous work,[28] an extended bibliographic research was required to choose suitable parameters for the plating kinetics. Few papers were published with a full set of values for both the intercalation and plating reactions and we see them varying strongly depending on different measurement techniques, used materials, or modeling purposes.

Table I collects available plating parameters published previously. The exchange current density, the activation energy, and the cathodic symmetry factor for the plating reaction are shown together with the different forms of the Butler–Volmer equation used. Where available, the intercalation kinetics are included, because the ratio of intercalation vs plating rate is an additional indicator on the consistency of the parameters. Some of the studies are based on modeling, others are purely experimental and used a wide range of different measurement techniques. Worth noticing that the plating kinetics is strongly influenced not only by the these last ones, as can be easily seen in the table, but also by the electrode characteristics in terms of dimensions[44] and morphology.[45] A detailed analysis of the strong relationship between different electrolyte compositions and lithium deposition kinetics can be found in some of the works[46–48] presented in Table I and is beyond the scope of this study in which the listed values have been specifically chosen to match our case.

Table I shows that, for the cathodic symmetry factor $\alpha_{c,Li}$, only two values are mainly used: a value of approx. 0.7 with reference to the experimental work of Verbrugge[44] and the renowned mathematical modeling work of Arora,[49] and a value of approx. 0.5 in many experimental works. The exchange current densities, however, scatter over many orders of magnitude, from 0.001 A m^{-2} to 1200 A m^{-2}. Interestingly, the most extreme values come from modeling work, while experimental data range "only" from 0.084 A m^{-2} to 316 A m^{-2}. Arora[49] explains the large variation in the values reported in literature with the difference in the surface conditions of the Li/Li cells under study and chooses as exchange current density the "standard" value of

Table I. Literature overview of experimental and modeling studies of lithium plating.

References	Type of study	Kinetic expressions for plating reaction	Exchange current density i^0_{Li}	Activation energy $E_{act,Li}$	Cathodic symmetry factor $\alpha_{c,Li}$	Intercalation kinetics i^0_{LiC6}	Activation energy E^{act}_{LiC6}
Arora (1999)[49] [at 21 °C]	Modeling (physics-based)	$i_{Li} = i^0_{Li}\left[\exp\left(\frac{\alpha_{a,Li}zF}{RT}\eta_{act}\right) - \exp\left(-\frac{\alpha_{c,Li}zF}{RT}\eta_{act}\right)\right]$	10 A m^{-2} [50]		0.7 [44]	2.1 A m^{-2}	
Verbrugge (1994)[41] [at 25 °C]	Experimental (Li/Li cell + voltammetry)	$i^0_{Li} = F(k_a)^{a_{c,Li}}(k_c)^{a_{a,Li}}(c_{Li})^{a_{a,Li}}$ $i_{Li} = i^0_{Li}\left[\exp\left(\frac{(1-\alpha_{c,Li})zF}{RT}\eta_{act}\right) - \exp\left(-\frac{\alpha_{c,Li}zF}{RT}\eta_{act}\right)\right]$	316 A m^{-2}		0.67		
Perkins (2012)[21] [at 25 °C]	Modeling (PDE + P2D models)	$j_{V,Li}(t) = a_{sn}i^0_{Li}\left[\exp\left(\frac{\alpha_{a,Li}zF}{RT}\eta_{act}(t)\right) - \exp\left(-\frac{\alpha_{c,Li}zF}{RT}\eta_{act}(t)\right)\right]$	10 A m^{-2}		0.7	0.96 A m^{-2} [a)]	
Ge (2017)[51] [at 25 °C]	Experimental (NMR) + P2D Modeling	$i^0_{Li} = k_{Li}(c_{Li^+[elyt]})^{\alpha_{a,Li}}$ $i_{Li} = \min\left\{0, i^0_{Li}\left[\exp\left(\frac{\alpha_{a,Li}zF}{RT}\eta_{act}\right) - \exp\left(-\frac{\alpha_{c,Li}zF}{RT}\eta_{act}\right)\right]\right\}$	0.17 A m^{-2} [a)]	35.3 kJ mol^{-1}	0.7[21,49]	1.17 A m^{-2} [a)]	45 kJ mol^{-1}
Ecker (2016)[14] [at 23 °C]	Experimental (Li/Li cell + EIS)	$i^0_{Li} = Fk_{Li}(c_{Li^+[elyt]})^{\alpha_{a,Li}}$ $i_{Li} = i^0_{Li}\left[\exp\left(\frac{\alpha_{c,Li}zF}{RT}\eta_{act}\right) - \exp\left(-\frac{(1-\alpha_{c,Li})zF}{RT}\eta_{act}\right)\right]$	20.4 A m^{-2}	65 kJ mol^{-1}	0.492	0.705 A m^{-2}	53.4 kJ mol^{-1}
Lueth (2015)[52] [at 25 °C]	Experimental (Li/Li cell + EIS)	$i^0_{Li} = \frac{R\cdot T}{z\cdot F\cdot A_e\cdot R_{ct}}$ $i_{Li} = i^0_{Li}\left[\exp\left(\frac{\alpha_{a,Li}zF}{RT}\eta_{act}\right) - \exp\left(-\frac{\alpha_{c,Li}zF}{RT}\eta_{act}\right)\right]$	1.758 A m^{-2}		0.7		
Tao (2017)[46] [at 23 °C]	Experimental (Li/Li cell + voltammetry)	$\log\frac{i_{Li}}{\exp\left(\frac{zF}{RT}\eta_{act}\right)-1} = \log i^0_{Li} - \frac{(1-\alpha_{c,Li})zF}{2.3RT}\eta_{act}$	21.7 ± 0.05 A m^{-2}		0.43 ± 0.05		
Lee (2002)[48] [at 25 °C]	Experimental (RDE + voltammetry)	$\frac{i_{Li}}{i^0_{Li}} = \left(1-\frac{i_{Li}}{i_{lim,c}}\right)\exp\left(-\frac{\alpha_{c,Li}zF}{RT}\eta_{act}\right)$	0.943 A m^{-2}		0.51		
Tippmann (2016)[22] [at−10 °C]	Modeling (P2D Newman-type)	$i_{Li} = i^0_{Li}\left[\exp\left(\frac{\alpha_{a,Li}zF}{RT}\eta_{act}\right) - \exp\left(-\frac{\alpha_{c,Li}zF}{RT}\eta_{act}\right)\right]$	1200 A m^{-2} [b)]		0.7 [49]		

Table I. (Continued).

References	Type of study	Kinetic expressions for plating reaction	Exchange current density i_{Li}^{0}	Activation energy $E_{act,Li}$	Cathodic symmetry factor $\alpha_{c,Li}$	Intercalation kinetics i_{LiC6}^{0}	Activation energy E_{LiC6}^{act}
Danner (2016)[24] [at 28 °C]	Modeling (3D microstructural)	$i_{Li} = i_{Li}^{0}\left[\exp\left(\frac{\alpha_{c,Li}zF}{RT}\eta_{act}\right) - \exp\left(-\frac{(1-\alpha_{c,Li})zF}{RT}\eta_{act}\right)\right]$ $i_{Li}^{0} = i_{Li}^{00}(c_{Li^+[elyt]})^{a_{c,Li}} (c_{Li})^{a_{c,Li}}(c_{Li}^{max} - c_{Li})^{1-a_{c,Li}}$	10 A m^{-2} [47]				
Meibuhr (1970)[47] [at 28 °C]	Experimental (Li/Li cell + polarization)	$i_{Li}^{0} = \frac{i_{Li}RT}{\eta_{iR-free\ polarization}}F$ $\eta_{iR-free\ polarization} = E_{exp} - E_{OC} - i_{Li}R$	9.5 ± 0.5 A m^{-2}		0.67		
Hein (2016)[25] [at 25 °C]	Modeling (3D microstructural)	$i_{Li} = i_{Li}^{0}\left[\exp\left(\frac{F}{2RT}\eta_{act}\right) - \exp\left(-\frac{F}{2RT}\eta_{act}\right)\right]$ $i_{Li}^{0} = i_{Li}^{00}(c_{Li^+[elyt]})^{0.5}$	12.6 A m^{-2} [53,54]		0.5	0.40 A m^{-2} [55,56]	68 kJ mol^{-1} [57]
Sequeira (1983)[58] [at 25 °C]	Experimental (Li/Li cell + polarization)	$i_{Li} = i_{Li}^{0}\left[\exp\left(\frac{(1-\alpha_{c,Li})zF}{RT}\eta_{act}\right) - \exp\left(-\frac{\alpha_{c,Li}zF}{RT}\eta_{act}\right)\right]$	12.6 A m^{-2}				
Yang (2018)[26] [at 0 °C]	Modeling (ECT model)	$j_{V,Li} = a_{sn}i_{Li}^{0}\left[\frac{c_{Li}}{c_{Li}^{0}}\exp\left(\frac{\alpha_{a,Li}zF}{RT}\eta_{act}\right) - \frac{c_{Li^+[elyt]}}{c_{Li^+[elyt]}^{0}}\exp\left(-\frac{\alpha_{c,Li}zF}{RT}\eta_{act}\right)\right]$ $i_{Li}^{0} = Fk_{Li}(c_{Li}^{0})^{\alpha_{c,Li}}(c_{Li^+[elyt]}^{0})^{\alpha_{a,Li}}$	50 A m^{-2} [c]		0.7 [49]	2.1 A m^{-2}	
Bieker (2015)[45] [at 20 °C]	Experimental (Li/Li cell + EIS)	Not available	0.084 A m^{-2} [a]				
Yang (2017)[27] [at 25 °C]	Modeling (ECT model)	$j_{V,Li} = -a_{sn}i_{Li}^{0}\exp\left[-\frac{\alpha_{c,Li}zF}{RT} \times \left(\Phi_s - \Phi_{elyt} - \frac{j_{tot}}{a_{sn}}R_{film}\right)\right]$	0.001 A m^{-2} [c]		0.5		
Present work [values at 23 °C]	Modeling (P3D)	$i_{Li} = i_{Li}^{0}\left[\exp\left(\frac{\alpha_{c,Li}zF}{RT}\eta_{act}\right) - \exp\left(-\frac{(1-\alpha_{c,Li})zF}{RT}\eta_{act}\right)\right]$ $i_{Li}^{0} = i_{Li}^{00}\exp\left(-\frac{E_{act,Li}}{RT}\right)\cdot\prod_{i=1}^{N_R} \times \left(\frac{c_i}{c_i^{0}}\right)^{(1-\alpha_{c,Li})}\prod_{i=1}^{N_P}\left(\frac{c_i}{c_i^{0}}\right)^{\alpha_{c,Li}}$	20.4 A m^{-2} [14]	65 kJ mol^{-1} [14]	0.492 [14]	2.81 A m^{-2} [28]	77.05kJ mol^{-1} [28]

a) calculated from values given in the reference. b) assumed value for modeling. c) adjusted value for modeling purposes (fitting parameter in absence of experimental data).

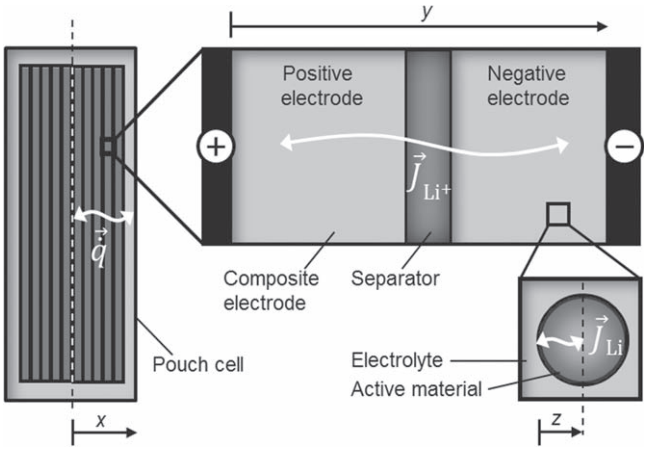

Figure 2. Schematic representation of 1D + 1D + 1D (pseudo-3D, P3D) modeling domain.

10 A m^{-2} reported in Jasinski[50] and Meibuhr[47] in the 1970 s. Excluding the high value found in Verbrugge[44] for an ultrahigh-rate lithium deposition on a microelectrode, the highest values found experimentally were obtained by Tao[46] and Ecker[14] (approx. 20 A m^{-2}).

It is interesting to compare the plating and the intercalation kinetics. In studies where parameters are available for both reactions, the exchange current density of the plating reaction at room temperature is around 10–25 times higher than that of intercalation, while the activation energies are in a similar range. Thus, given the same overpotentials, plating is considerably faster than intercalation.

Only in the work of Ecker[14] and Ge[51] a full set of parameters including the activation energy, and both for plating and intercalation reactions, is given. The Li/Li coin cell used by Ecker[14] for the model parametrization consists of two metallic lithium foils and a separator coming from a 7.5 Ah high-energy Kokam cell together with 1M $LiPF_6$ in EC/EMC (1:1 wt) electrolyte. Because of these similarities with our reference cell, we selected the plating kinetic parameters of Ecker[14] in the present model. When given a complete set of parameters, it is possible to calculate i^0 for both the reactions at different temperatures. Obviously our present work and Ecker[14] show identical values for i^0_{Li} at 25 °C (24.3 A m^{-2}) and −10 °C (0.74 A m^{-2}), being the parameters for the plating reaction the same. Nevertheless, i^0_{LiC6} values are quite different at 25 °C (3.47 and 0.81 A m^{-2}) and quite similar at −10 °C (0.06 and 0.05 A m^{-2}) for the two studies. The ratios $i^0_{Li}/i^0_{LiC_6}$ of exchange current density of plating reaction to that of intercalation reaction are at 25 °C 7 and 30, respectively in our work and Ecker, but at −10 °C the difference between the ratios in the two studies gets remarkably smaller, respectively 12 and 15.

In summary, at low temperatures both the plating and intercalation reactions are considerably slowed down as compared to room temperature. Still, the exchange current density of plating remains an order of magnitude faster than that of intercalation. Therefore, intercalation overpotentials can be high and drive the anode potential below the thermodynamic plating limit, where intercalation can then become fast.

Modeling and Simulation Methodology

Pseudo-3D model.—The study presented here is based on a modeling framework previously developed about a commercial 350 mAh high-power lithium-ion pouch cell with graphite at the anode and NCA/LCO blend at the cathode. A description of the development and parametrization of the model is available in Carelli et al.[28] and the transport equations were derived in Kupper et al.[43] A summary of all model equations as well as symbol definitions are given in the Appendix.

Figure 2 illustrates schematically the 1D + 1D + 1D (pseudo-3D or P3D) multiscale modeling domain. The transport scales combine heat transport through the cell thickness (in this paper referred to as macroscale or x scale), mass and charge transport inside the liquid electrolyte (mesoscale, y scale), and diffusive mass transport in the active material (AM) particles (microscale, z scale). Main assumptions of the transport model are: (a) Heat transport on the macroscale is assumed conductive, and heat losses at the boundaries are modeled as combined convective and radiative. Differently from the previous model,[28] the heat transport is here assumed symmetrical to the center of the cell ($x = 0$), and the cell surface is exposed to ambient air without additional cell holder; (b) on the mesoscale, the electrodes are described in a continuum setting, that is, microstructure is not resolved; (c) on the microscale, lithium transport in the AM is modeled by Fickian diffusion with stoichiometry-dependent diffusion coefficient; (d) the three scales are coupled through boundary conditions and chemistry and heat source terms.

Electrochemistry.—Our model previously developed[28] was extended to include the plating reaction Eq. 1 as additional reaction (side reaction) at the anode with the purpose of simulating reversible lithium plating. As will be shown below, for some simulations we included an additional reversible re-intercalation reaction,

$$\mathrm{Li[metal]} + \mathrm{V[C_6]} \rightleftharpoons \mathrm{Li[C_6]}. \qquad [11]$$

This reaction takes place at the contact interface between plated lithium and graphite. Table II summarizes all reactions and their kinetic coefficients used in the present model. All charge-transfer reactions are modeled with Butler-Volmer kinetics (Eq. 10). At the anode, intercalation, plating and re-intercalation are assumed to take place in parallel. The kinetic parameters are area-specific, and we assume that all three reactions take place at the same surface (the graphite/electrolyte interface). In the present model, the reaction surface area is assumed constant and independent of lithium volume fraction. Therefore, the present model does not consider effects like blocking of the graphite surface by metallic lithium or detachment of metallic lithium fragments. These effects will be considered in future investigations.

All three intercalation materials (graphite at the anode, LCO and NCA at the cathode) are characterized by their lithium stoichiometry X_{Li}. The balancing of the electrodes (i.e., values for X_{Li} corresponding to 0% and 100% SOC) was determined previously by fitting half-cell potential curves to a measured full-cell quasi-OCV curve.[41] For graphite, a value of $X_{Li[C6]} = 0.619$ was obtained for 100% SOC. Therefore, the anode is significantly oversized in the cell studied here.

The model framework includes a continuity equation for all solid, liquid and gaseous phases present in the electrode, allowing to track formation and growth of new phases, such as the plated lithium in the anode. In the continuum setting, all phases are characterized by their respective volume fractions. We therefore include lithium metal as additional phase at the anode, and its starting volume fraction is set to an initial value of 10^{-11}. As metallic lithium grows, the electrode porosity is reduced accordingly. Specific care must be taken when calculating reversible reaction rates of phase formation/decomposition reactions, such as the plating reaction, Eq. 1. For a stoichiometric (single-component) phase like metallic lithium, the activity of lithium is constant equal to unity, as long as this phase is present. When the phase becomes completely consumed (reverse reaction Eq. 1, e.g. during re-intercalation), the activity shows a non-monotonous drop to zero. In the present model, we define a limiting lithium volume fraction of 10^{-10}, below which the decomposition rate is set to zero.

Model parameterization.—The parameterization of electrochemical models is one of the key factors in building up a reliable and working model, given the number of parameters and their dependence on operating conditions. In particular, we require (1)

Table II. Interfacial chemical reactions and rate coefficients used in the present model.

Interface	Reaction	Label	Rate coefficient	Activation energy $E_{act,f}$/kJ mol^{-1}	Symmetry factor α_f
Graphite/electrolyte (anode)	$Li^+[elyt] + e^- + V[C_6] \rightleftarrows Li[C_6]$	Intercalation	$i^{00} = 8.84\ 10^{14}$ A m^{-2}	77.1	0.5
Graphite/electrolyte (anode)	$Li^+[elyt] + e^- \rightleftarrows Li[metal]$	Plating	$i^{00} = 2.29\ 10^{13}$ A m^{-2}	65.0	0.492
Graphite/electrolyte (anode)	$Li[metal] + V[C_6] \rightleftarrows Li[C_6]$	Re-intercalation	$k_f = 1\ 10^{-6}$ m^3/(mol·s)[a)]	0[a)]	—
LCO/electrolyte (cathode)	$Li^+[elyt] + e^- + V[LCO] \rightleftarrows Li[LCO]$	Intercalation	$i^{00} = 8.20\ 10^{12}$ A m^{-2}	72.3	0.5
NCA/electrolyte (cathode)	$Li^+[elyt] + e^- + V[NCA] \rightleftarrows Li[NCA]$	Intercalation	$i^{00} = 2.63\ 10^{10}$ A m^{-2}	61.0	0.5

a) Arbitrary values, set fast.

thermodynamic data of all species involved (molar enthalpies and entropies including their dependence on lithium stoichiometry in case of intercalation materials); (2) kinetic data of all reactions (pre-exponential factors, activation energies and symmetry factors); (3) physical data of all phases (phase densities or species molar volumes); and (4) structural parameters (electrode thicknesses, volume fractions, etc.). For the base model of the 0.35 Ah graphite/NCA-LCO cell studied here, these parameters were compiled in our previous paper.[28] For the present extension, we therefore require only the parameters related to the lithium plating reaction and the lithium metal phase. This was described in the previous Section.

Simulation methodology.—The P3D model above is an extension of the framework already presented in Carelli et al.[28] The governing equations were implemented in the in-house multiphysics software package DENIS (Detailed Electrochemistry and Numerical Impedance Simulation)[43] and numerically solved using the implicit time-adaptive solver LIMEX.[59,60] The chemical thermodynamics and kinetics are evaluated with the open-source code Cantera[61] (version 2.5.0a3), which is coupled to the DENIS transport models via the chemistry source terms. An in-depth explanation about the software can be found in Mayur et al.[40] The lithium metal phase is described through Cantera's *StoichSubstance* class *(stoichiometric_solid)*, with density kept constant to a value of 534 g cm^{-3} [62] The Cantera input file is available from the authors upon request. In order to set the activity of vanishing phases to zero, we use Cantera's *phaseExistence* functionality implemented in the *interfaceKinetics* class. MATLAB (version 2019a) is the chosen interface for controlling all DENIS simulations, as well as for data evaluation and visualization.

Experimental data.—An adequate way to validate a multi-scale cell model is by comparison to macroscopic cell experiments: in our case, cell voltage and current measurements at low temperatures and/or high C-rates (conditions for plating at the anode). In this study two cases are exposed and simulations from two slightly different models (with and without re-intercalation reaction) were carried out and compared to two different sets of experiments.

In the first case ("Kokam 0.35 Ah"), cell-level experiments on our reference cell[28] (0.35 Ah high-power Kokam pouch cell with LCO/NCA blend cathode) were carried out in order to obtain validation data for our model. Electrical tests (Biologic) were carried out with two individual cells in a climate chamber (CTS T-40/200 li) with the purpose of detecting the two most common plating hints (voltage plateau and voltage drop).

In the second case ("Kokam 40 Ah"), we used experimental data shown by Ecker[14] for a 40 Ah high-power Kokam cell. This reference has also been used to parametrize the plating reaction and as guideline for our own experimental protocols. According to the manufacturer, the cell studied by Ecker comprises graphite at the anode, NMC at the cathode and an EC/EMC mixture with $LiPF_6$ as electrolyte. Even if our modelled cell has a different format and cathode chemistry, the graphite anode may be sufficiently similar (same manufacturer, same high-power characteristics) to allow for comparison. Indeed the model is able to adapt and simulate successfully both cases, as will be shown and explained in the following Section.

Comparison of Simulations with Experiments

In the following Subsections, two different sets of experiments ("Kokam 0.35 Ah" and "Kokam 40 Ah") are shown and compared to simulations. Both cells show a qualitative difference in low-temperature charging behavior. Only a *voltage drop* seemed lightly visible for "Kokam 0.35 Ah", while both *voltage drop* and *voltage plateau* are very evident for "Kokam 40 Ah". We had to adapt the model in order to predict these differences. In the Subsections about "Kokam 0.35 Ah" , the modeling framework includes three reactions at the anode, that is, intercalation, plating and re-intercalation. A parametric study of the rate coefficients was carried out in order to understand the mutual influence of the three competing reactions. In the Subsection about "Kokam 40 Ah", the model includes only the intercalation and plating reactions and successfully reproduces both plating hints.

Kokam 0.35 Ah—charge/discharge at constant temperature.—The protocol used in this Section was chosen to probe the potential presence of a *voltage plateau* of a plated cell during discharge. Specifically, starting from a fully-discharged cell, we apply a 1C CC charge—45 min CV charge—30 min rest—1C CC discharge protocol both in experiments and simulations at a constant ambient temperature of −10 °C. Figure 3 compares the results. All panels show a set of simulated curves that were obtained with different kinetics of the plating reaction, keeping all other parameters constant. The base value of the exchange current density (rate factor 1) is given in Table II, as derived from the literature survey discussed above. Simulations with other rate factors (0.01, 0.1, 10, 100) help us understanding how the plating kinetics influences the cell behavior. Because the duration of the CC charge phase is strongly affected by the choice of the rate factor, we have decided to set the time scale to zero at the beginning of the CV phase to allow a better visual comparison for the different charge/discharge phases.

The left part of Fig. 3 shows simulations obtained with a modeling framework consisting only of intercalation and plating (re-intercalation reaction switched off). Panel a) shows the cell voltage: except for a rate factor of 0.01, all simulations show a more or less pronounced *voltage plateau* both in the CC charge and in the CC discharge phases, while this plating hint looks totally absent in the experiments. Worth noticing also how the different rates affect the CC phase and the voltage during the rest. Panel b) shows the current density (negative for charge). Panel c) shows the macroscopic SOC of the cell, obtained by Coulomb counting. The maximum SOC of the cell strongly depends on plating kinetics: faster plating leads to a higher apparent (Coulomb-counting based) SOC. Figure 3d shows the simulated volume fraction of metallic lithium (averaged over the anode thickness): easy to see how much plating is affected by its kinetics, with lithium formation starting in the last part of the CC phase (corresponding to the CC voltage plateau during charging for the factors from 1 to 100), the peak in different moments of the CV charge (with 0.01 and 0.1 pushed towards the end of this phase) and then the decrease back to zero during the discharge due to the reversible plating reaction. Finally, the temperature in Panel e) shows self-heating/cooling effects as combination of reversible and irreversible heat sources, as was discussed in detail in Carelli et al.[28]

As already noted, the experimental discharge voltage curve does not show any particular plateau while this is clearly visible in 4/5 of the plotted simulations. This is why we decided to add an extra reaction to include re-intercalation. The kinetics of the re-intercalation reaction were set fast (Table II) and not rate-limiting. The results are shown in the right part of Fig. 3. In Panel f), the simulations do not show any voltage plateau during the CC discharge and the voltage during the rest phase looks lower, showing the best match with the experiments at the standard plating rate. Yet, the voltage plateau during CC charge is still present. Panel g) and h) show respectively the current density and the SOC: it is remarkable that these curves are very similar to the case without re-intercalation (left panel). In Panel i), showing the simulated lithium volume fraction, only plating rate factors of 100 and 10 (and much less evidently 1) seem to allow the formation of plated lithium, with the decrease happening during the CV and the rest phase. This is probably the reason behind the absence of a voltage plateau even at the highest plating rates. The temperatures shown in Panel j) show no important differences with corresponding Panel e).

For a better understanding of the two mechanism (without and with re-intercalation reaction), we can consider the rate of progress of the involved reactions. In Fig. 4 we show data for simulations at

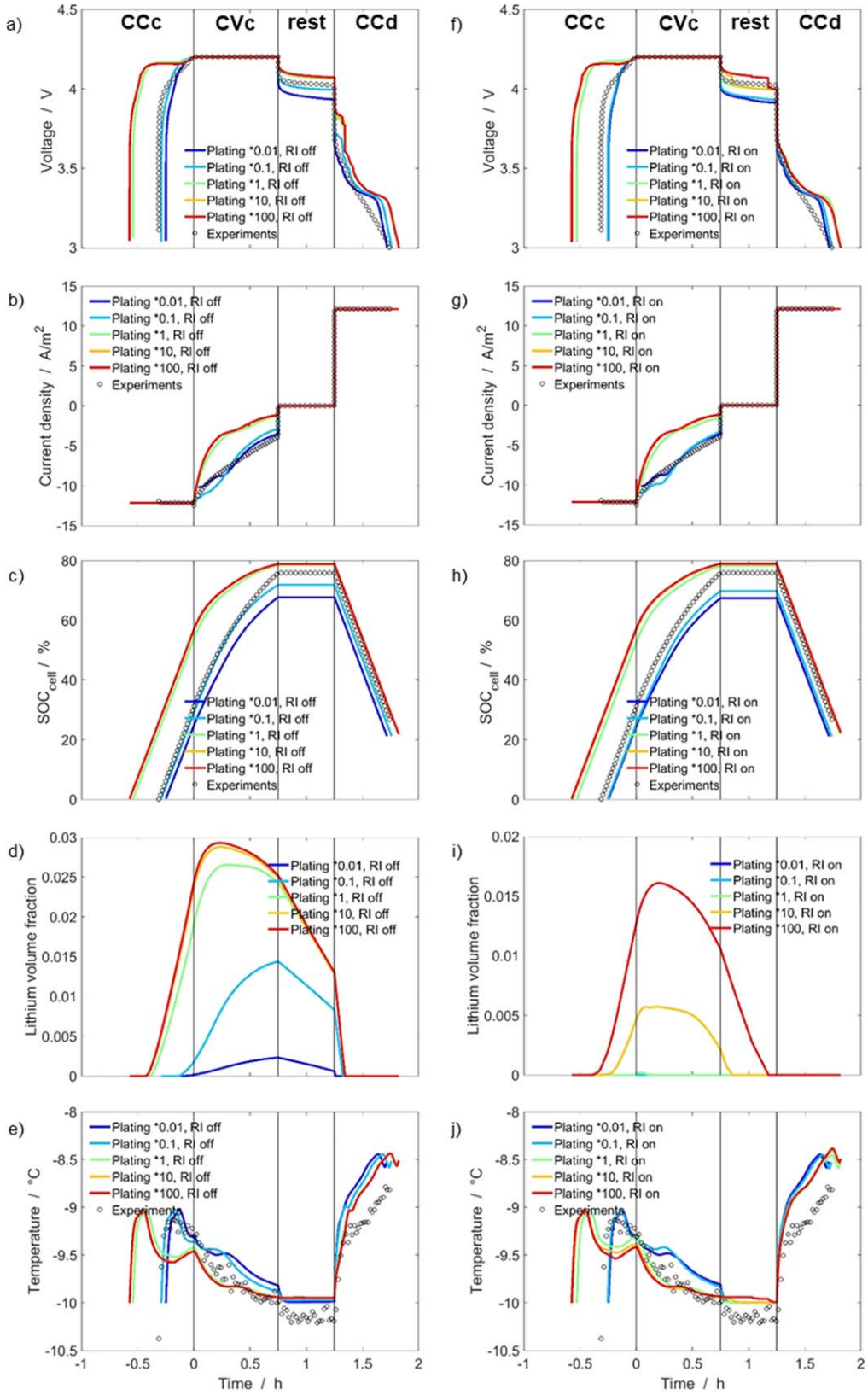

Figure 3. Simulations and experimental data for charge (1C CC, 45 min CV)—rest (30 min)—discharge (1C CC) at constant ambient temperature of −10 °C and multiplying rate factors for the plating kinetics varying from 0.01 to 100. On the left, with re-intercalation reaction off: (a) voltage, (b) current density, (c) cell SOC, (d) lithium volume fraction, (e) temperature. On the right, with re-intercalation reaction on: (f) voltage, (g) current density, (h) cell SOC, (i) lithium volume fraction, (j) temperature.

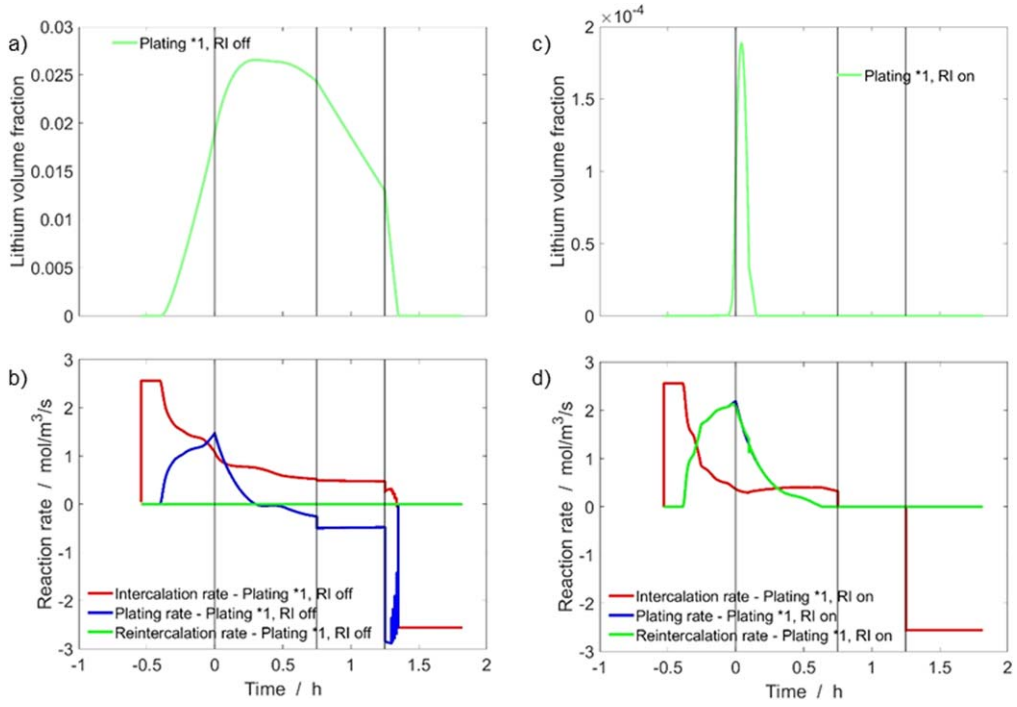

Figure 4. Simulations for a charge (1C CC, 45 min CV)—rest (30 min)—discharge (1C CC) at constant temperature of −10 °C and standard plating rate (rate factor 1). On the left, with re-intercalation reaction off: (a) lithium volume fraction, (b) reaction rates of progress. On the right, with re-intercalation reaction on: (c) lithium volume fraction, (d) reaction rates of progress.

standard plating rate (rate factor 1), that has been seen to be the best match with our experimental data. The left and right columns show simulations without and with re-intercalation reaction, respectively; the upper row shows lithium volume fraction and the lower row the rates of progress of the three reactions. Without the re-intercalation reaction (panel b), the plating rate peaks at the end of the CC charge, starting its decrease during the CV phase and becoming negative at 0.3 h. The intercalation rate remains positive throughout the rest phase and even into the CC discharge until the end of the voltage plateau at around 1.3 h. During the rest phase, when there is no external current applied, intercalation and plating show opposite rates with same magnitude. This shows that, even without an explicit re-intercalation reaction, re-intercalation of plated lithium takes place via these two reactions.

In Panel d) of Fig. 4 we consider instead the model with the reversible re-intercalation reaction included. Here, the intercalation rate drops to 0 at the end of the CV charge and therefore vanishes as soon as the externally-applied current vanishes. The plating rate peaks at the end of the CC charge, as in Panel b). However, the re-intercalation reaction shows almost the identical rate as the plating reaction, which means that all formed metallic lithium is quickly re-intercalated. This results in only a small lithium volume fraction (panel c). Moreover, the plating rate never becomes negative.

Kokam 0.35 Ah—rest with temperature change.—Next, we applied a protocol typical for probing a potential *voltage drop* of a plated cell after heat-up. In Fig. 5 simulations are compared with experimental data for a rest (30 min)—charge (1C CC, 45 min CV)—rest (3.5 h) including temperature rise to 25 °C—discharge (1C CC) protocol. The CCCV charge started with a fully-discharged cell and was carried out at an ambient temperature of −10 °C. The rest phase consisted of first a 30 min wait phase at the same temperature, then heating to 25 °C. The final CC discharge takes place at constant temperature of 25 °C.

The same parameter variation was carried out as in the previous Section. The left part of Fig. 5 shows simulations obtained with a modeling framework without re-intercalation reaction. In Panel a) both the experiment and the simulations show a small *voltage drop* during the heating of the cells (about 50 mV in the experiments), exactly 30 min after the first drop corresponding to the beginning of the rest phase. This drop is more or less enhanced in the simulations depending on plating kinetics, with the best match with the experimental data happening to be with a rate factor of 0.1. The voltage drop is one of the plating hints detected when cells are charged at low temperatures and then heated during the following rest[14–17] but in this case the drop is not so evident as often seen in literature. Worth noticing also how the different rate factors affect the CC phase and the voltage during the rest. Panel b) shows the current density (negative for charge) and Panel c) shows the SOC of the cell. Panel d) shows the simulated volume fraction of metallic lithium (averaged over the anode thickness). Again, plating kinetics strongly affects Li formation. In Panel e) the temperature behavior is dominated by the temperature rise at around 1.2 h.

On the right side of Fig. 5, simulations obtained with the same modeling framework but including the re-intercalation reaction are shown. In Panel f), the simulated voltage drop during heating seems flattened but still visible, with the best match with the experiments for the standard plating rate (factor 1). For the highest rate factor, the drop keeps the same height as seen in Panel a) but looks shifted in time, which can be explained with the simulated re-intercalation happening now earlier and not anymore connected to the time of the temperature rise. Panel g) and h) show respectively the current density and the average SOC: in both panels only rate factors of 0.1 and 1 look slightly affected by the re-intercalation reaction. In Panel i), showing the simulated volume fraction, only rate factors of 100 and 10 (and much less evidently 1) seem to allow the formation of plated lithium, with the decrease happening during the CV (rate factor 10) and the rest phase (rate factor 100). Panel j) shows no significant differences with corresponding Panel e).

Figure 6 shows lithium volume fraction and reaction rates of progress for a standard plating rate (rate factor 1). Panel b) shows reaction rates for the model without re-intercalation reaction. After

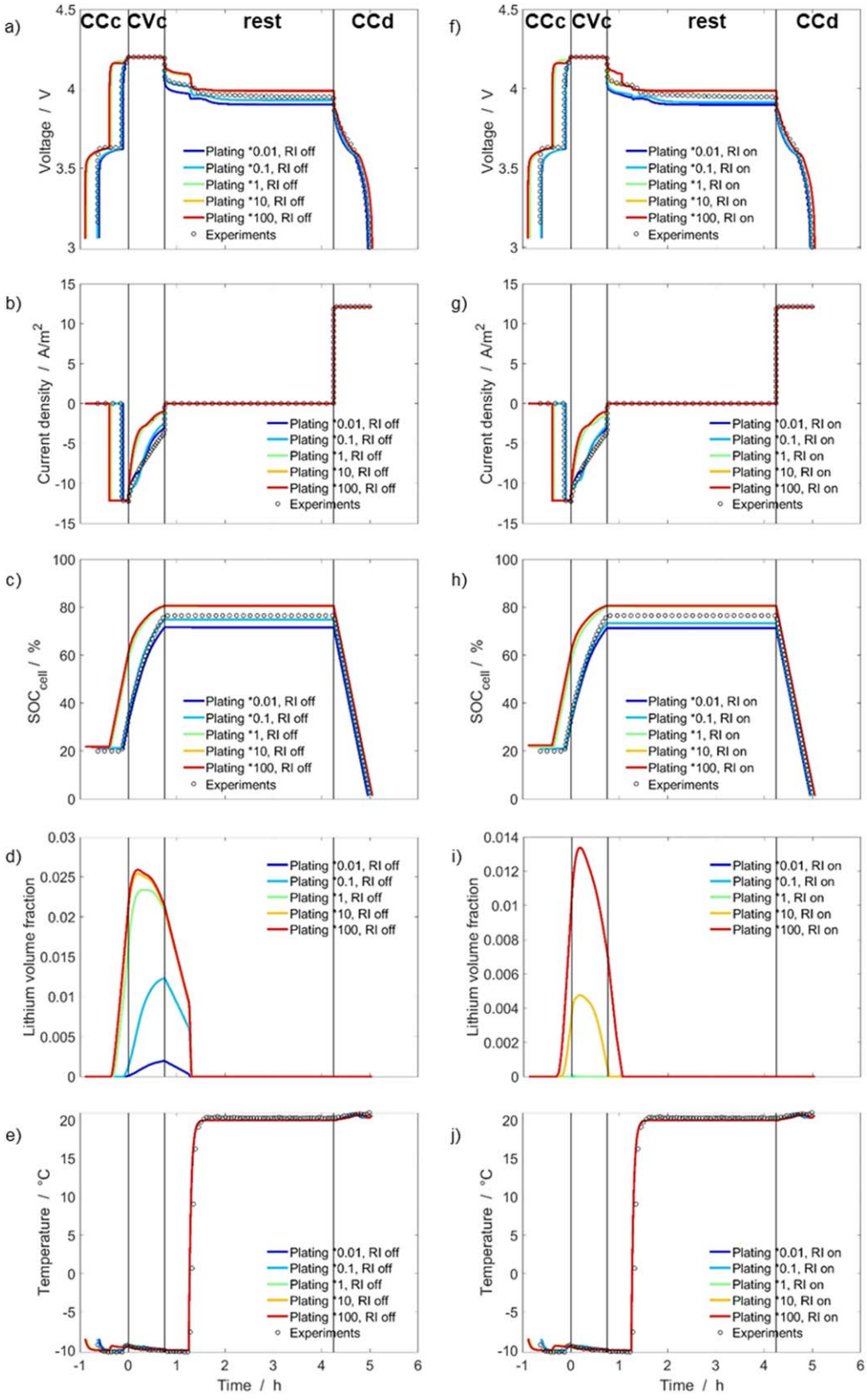

Figure 5. Simulations and experimental data for a rest (30 min)—charge (1C CC, 45 min CV)—rest (3.5 h including temperature rise to 25°C)—discharge (1C CC) cycle at initial temperature of −10 °C and varying plating rate factors from 0.01 to 100. On the left, with re-intercalation reaction off: (a) voltage, (b) current density, (c) cell SOC, (d) lithium volume fraction, (e) temperature. On the right, with re-intercalation reaction on: (f) voltage, (g) current density, (h) cell SOC, (i) lithium volume fraction, (j) temperature.

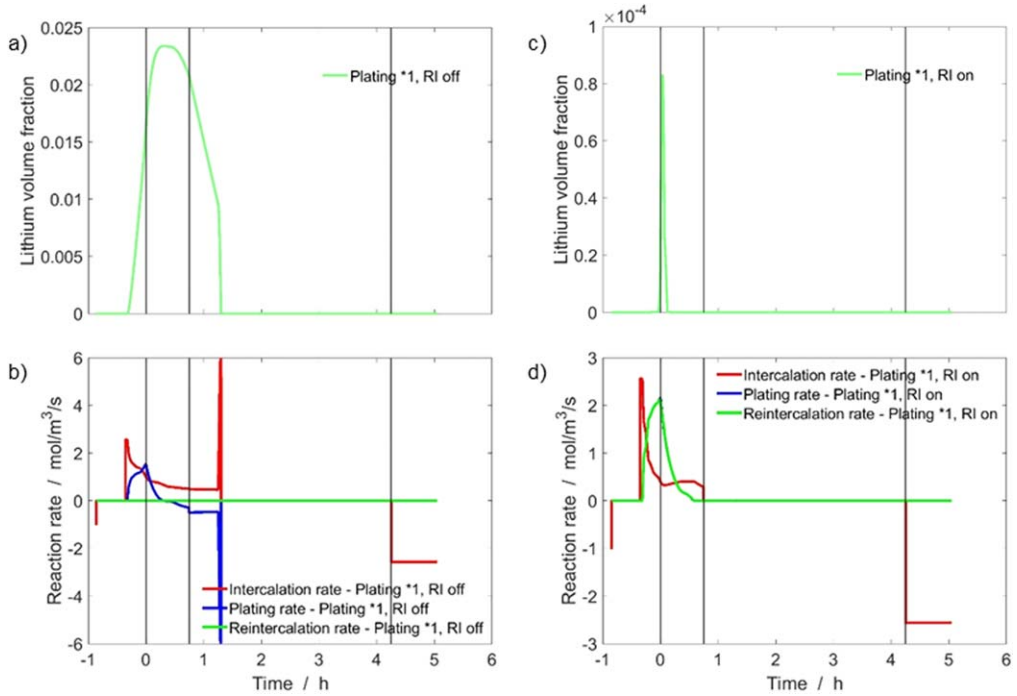

Figure 6. Simulations for rest (30 min)—charge (1C CC, 45 min CV)—rest (3.5 h including temperature rise to 25 °C)—discharge (1C CC) cycle at initial temperature of −10 °C and standard plating rate (rate factor 1). On the left, with re-intercalation reaction off: (a) lithium volume fraction, (b) reaction rates of progress. On the right, with re-intercalation reaction on: (c) lithium volume fraction, (d) reaction rates of progress.

reaching the maximum, the plating rate drops quickly to negative values, staying stable during the first rest phase and then reaching the maximum negative during the voltage drop, while the intercalation rate remains positive and shows a sharp peak equal and inverse to plating. Panel d) shows very clearly how much adding the re-intercalation reaction in the model has an influence on the other reactions rates of progress. The intercalation rate drops to zero at the end of the CV charge and the plating rate never becomes negative, which means the plated lithium formed during the charge gets simply irreversibly re-intercalated through the additional reaction: this is easily visible in the plot, where the re-intercalation is essentially superimposed to the plating rate. From the observation of the panels on the right of Fig. 6, it is then possible to speculate the small voltage drop seen in our experiments being likely due to the temperature rise and corresponding equilibration of the intra-particle lithium gradients, and not due to re-intercalation.

The data shown in Figs. 5 and 6 demonstrate the challenges in interpreting plating hints when multiple reactions and external factors like the temperature are involved. The absence of a voltage plateau and the characteristics of the voltage drop here analyzed are therefore indicative of a cell less likely to be affected by plating, whose modeling requires the adding of an explicit re-intercalation reaction to suppress the otherwise expected plating hints.

Kokam 40 Ah—charge/discharge at constant temperature and rest with temperature change.—In this Section, we compare our model to Ecker's experimental data,[14] in which both the *voltage plateau* and *voltage drop* are clearly visible. Although that cell has a different format and chemistry, a qualitative comparison reveals further insight. In all simulations shown here, the re-intercalation reaction was switched off, leaving only intercalation and plating as reactions at the anode.

Figure 7 compares simulations and experiments. On the left, a CC charge-discharge cycle (1C/1C) at constant ambient temperature −10 °C is shown. Panel a) shows simulated cell voltage and cell surface temperature and Panel b) shows the corresponding C-rate (positive for charge) and the simulated average SOC of the anode, defined as

$$\mathrm{SOC}_{\mathrm{avg}} = \frac{\overline{\overline{X}}_{\mathrm{Li,an}} - X^{\mathrm{min}}_{\mathrm{Li,an}}}{X^{\mathrm{max}}_{\mathrm{Li,an}} - X^{\mathrm{min}}_{\mathrm{Li,an}}}, \qquad [12]$$

where the stoichiometry $\overline{\overline{X}}_{\mathrm{Li,an}}$ is averaged over both the anode thickness and the particle diameters (y and z scales, respectively, cf. Fig. 2), and the nominal stoichiometry ranges $X^{\mathrm{min}}_{\mathrm{Li,an}}$ and $X^{\mathrm{max}}_{\mathrm{Li,an}}$ are given in our previous work.[28] Therefore, different to the previous Sections, this is a chemical instead of an electrical SOC.

In Panel a) the simulation and the experiment show characteristic *voltage plateaus* during the charge and during the discharge. Self-heating of the cell leads to nearly a 7 °C rise during the cycle. Both voltage and temperature show qualitative agreement between model and experiment, although the discharge plating plateau in the experiments extends towards larger times than in the model. The observed plateau at discharge is one of the plating hints often found in cells after charge at low temperatures.[5–14] In Panel b), the simulated chemical SOC of the anode and the C-rate are shown. We observe that the anode SOC continues increasing even after we switch from charge to discharge, and only continues decreasing after having bypassed the plateau zone. It is interesting to note the nonlinearity of the SOC and its asymmetry with respect to charge and discharge, both caused by the presence of plating.

Our model allows an in-depth analysis of the processes inside the cell during this plateau. Panel c) shows the metallic lithium volume fraction. Plating starts at around 0.15 h, simultaneously with the occurrence of the charge voltage plateau. Metallic lithium peaks at end of charge at 2.1 vol.-%, which is quite significant, and then decreases during the discharge plateau. Panel d) shows intercalation and plating reaction rates, showing again the onset of plating. After switching to discharge, the plating rate becomes negative, while the intercalation rate remains positive, consistent with the continuous increase of anode SOC. The absolute value of the plating reaction rate is larger than that of intercalation, showing that metallic lithium is simultaneously oxidized (Li^+[elyt] + e^- ⇄ Li[metal]) and re-intercalated a solution-mediated mechanism as discussed below.

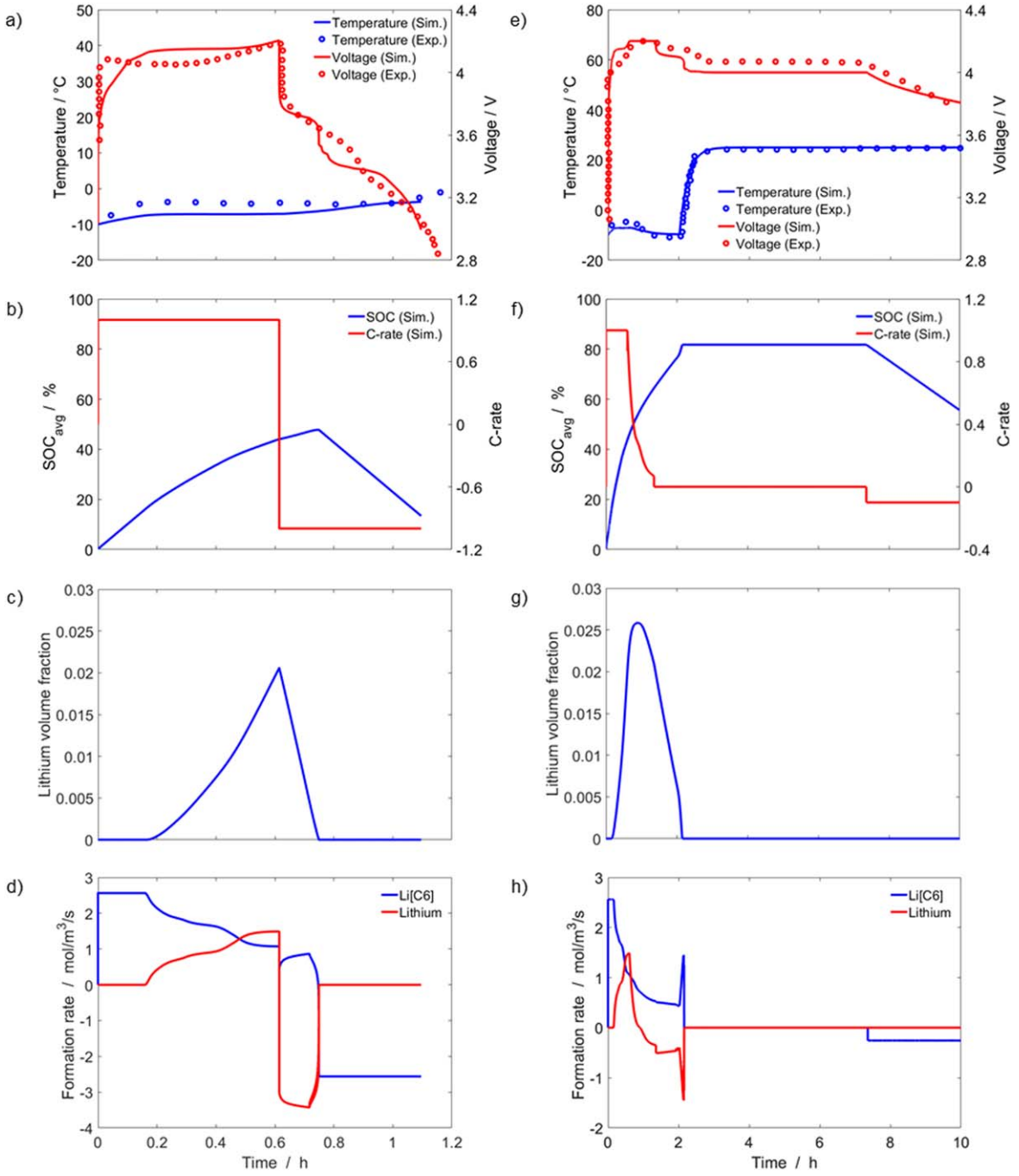

Figure 7. Simulations (this work) and experimental data (Ecker[14]). On the right, a charge-discharge cycle (1C/1C) at constant ambient temperature of −10 °C: (a) voltage and temperature, (b) SOC and C-rate, (c) lithium volume fraction, (d) formation rates $\dot{s}_{\mathrm{LiC6}}$ and $\dot{s}_{\mathrm{Li}}$. On the left, a charge (1C CCCV)—rest (6 h including temperature rise to 25 °C)—discharge (0.1C CC, here only partially shown) cycle at initial temperatures of −10 °C: (e) voltage and temperature, (f) SOC and C-rate, (g) lithium volume fraction, (h) formation rates $\dot{s}_{\mathrm{LiC6}}$ and $\dot{s}_{\mathrm{Li}}$.

In the right panels of Fig. 7, a CCCV charge (1C) at low temperature, followed by a rest period with temperature rise to room temperature, and subsequent CC discharge (0.1C) is shown. The CCCV charge was at −10 °C and the rest phase consisted of first a 30 min wait phase at the same temperature, then heating of the cells to 25 °C with an additional 5.5 h. The final CC discharge takes place at constant temperature of 25 °C. In Panel e), both the experiment and the simulation show a clear *voltage drop* (about 100 mV—two times the drop seen in "Kokam 0.35 Ah – rest with temperature change") during the heating of the cells, more enhanced in the simulated data and exactly 30 min after the first drop corresponding to the beginning of the rest phase. A small voltage plateau in the last part of the CC charge is also clearly visible in the simulation and corresponds to the same plateau that is visible in Fig. 7a. In this case, the voltage drop is not due to the temperature rise of the cell, but to the re-intercalation of the plated lithium formed during charge, which is frozen out at low temperatures. Again, our model allows us to analyze the internal states of the cell. Figure 7f shows the chemical SOC of the anode and the C-rate. We can actually observe that the SOC continues increasing even during the first rest phase and accelerates when heating to 25 °C, to then stay stable once all the plated lithium has been re-intercalated (corresponding to the

second voltage drop) and normally decrease during CC discharge. Panel g) shows the metallic lithium volume fraction. Plating starts at around 0.15 h, simultaneously with the occurrence of the small charge voltage plateau. Metallic lithium reaches the peak at 2.7 vol.-% during the CV charge and then starts decreasing to 0, with increased rate during the heating of the cell and the corresponding voltage drop. This is clearly visible in Fig. 7h, which shows intercalation and plating reaction rates. After reaching the maximum, the plating rate drops quickly to negative values, staying stable during the first rest phase and then reaching the maximum negative during the voltage drop, while the intercalation rate remains positive and shows a sharp peak equal and inverse to plating. This is consistent with the anode SOC and shows clearly how the re-intercalation tends to happen already in the CV phase and to be accelerated by warm temperatures.

Discussion.—In the Sections above we have compared simulated cell behavior with experiments from two different cell types and applying different operation protocols. The simulations demonstrate the highly complex competition of intercalation, plating and potential re-intercalation reactions, leading to distinct features in the macroscopic cell behavior such as voltage plateaus and drops. The observed macroscopic behavior can be explained by analyzing the internal states (reaction rates of progress, species formation rates, lithium volume fraction) of the physicochemical model.

The model was originally parameterized to represent the "Kokam 0.35 Ah" cell. However, none of the kinetic mechanisms investigated here was able to reproduce the experimental data over the complete charge-rest-discharge cycle. The best reproduction of the experimental data could be obtained with the addition of a reversible re-intercalation reaction. This was necessary as the experiments do not show clear plating hints, despite the fact that the cell was operated well into a regime usually known to induce plating. When varying the kinetics of the plating reaction, best agreement with experiments was observed with the "standard" rate, confirming the conclusions of our literature research.

It interesting that, when comparing the model to the experiments of the "Kokam 40 Ah" cell, good qualitative agreement could be achieved; in particular, the plating hints could be clearly reproduced without requiring the explicit addition of a re-intercalation reaction. Quantitative differences between experiment and model are expected due to the different chemistry and size of the investigated cells (0.35 Ah NCA/LCO cathode simulated and 40 Ah NCM cathode experimental); taken this difference into account, the qualitative agreement is rather remarkable.

The introduction of the re-intercalation reaction was shown to strongly affect the simulation results. This can be explained as follows. In the simpler mechanism consisting of only intercalation and plating, we have observed that re-intercalation of plated lithium is still possible, for example during the rest phase, as the two reactions can operate in parallel but opposite directions according to

$$\mathrm{Li[metal]} \rightarrow \mathrm{Li^+[elyt]} + \mathrm{e^-} \qquad [13]$$

$$\mathrm{Li^+[elyt]} + \mathrm{e^-} + \mathrm{V[C_6]} \rightarrow \mathrm{Li[C_6]}. \qquad [14]$$

We can refer to this mechanism as *solution-mediated re-intercalation*, because electrolyte-dissolved lithium ions are formed as intermediates. As soon as we explicitly add a re-intercalation reaction, we open up the possibility of a *surface-mediated re-intercalation* according to

$$\mathrm{Li[metal]} + \mathrm{V}[C_6] \rightarrow \mathrm{Li[C_6]}. \qquad [15]$$

Although this reaction is merely the sum of Reactions (13) and (14), it follows a different physicochemical behavior; for example, it is independent of electrical potential (cell voltage).

The present framework does not include any morphological model of plated lithium. However, we expect the morphology to have a strong influence on the re-intercalation behavior. The solution-mediated re-intercalation mechanism requires a large lithium/electrolyte interfacial area and is therefore more likely to occur in dendrite-like structures. The surface-mediated re-intercalation mechanism, on the other hand, requires direct contact between lithium and graphite and is therefore more likely to occur in film-like structures. The two mechanisms studied here (re-intercalation off and on) can therefore also be interpreted as two limiting cases for lithium morphology (dendrite-like and film-like, respectively).

A tentative interpretation of the different behavior of the two investigated cells is therefore as follows. The "Kokam 0.35 Ah" cell shows a film-like lithium growth, therefore allowing surface-mediated re-intercalation and showing little plating hints in the macroscopic voltage behavior. The "Kokam 40 Ah cell," on the other hand, shows a dendrite-like lithium growth, therefore allowing mainly only solution-mediated re-intercalation and consequently showing strong plating hints in the macroscopic voltage behavior.

Plating Simulations

After the comparison between simulations and various experimental data sets, we now use the model for a detailed analysis of the cell behavior, including the further investigation of internal gradients, and the discussion of degradation maps. Throughout this Section, we use a model with the simpler mechanism consisting of only intercalation and plating at the anode, that is, no explicit re-intercalation reaction.

Spatiotemporal analysis.—In this Section we discuss the simulated internal cell states during 1C CC charge and 1C CC discharge at +10 °C and −10 °C. The conditions and simulation methodology are the same as described in "Kokam 40 Ah - charge/discharge at constant temperature and rest with temperature change" where we detected the *voltage plateau* as plating hint. The comparison at +10° in absence of plating[14] has been added to better understand the effect of temperature on the internal states.

On the mesoscopic scale, that is, along the electrode pair thickness, the spatiotemporal behavior of metallic lithium volume fraction and local SOC is shown for a CC charge in Fig. 8 and for a subsequent CC discharge in Fig. 9. Here, the local SOC is defined as

$$\mathrm{SOC_{local}}(y) = \frac{\bar{X}_{\mathrm{Li,an}} - X^{\mathrm{min}}_{\mathrm{Li,an}}}{X^{\mathrm{max}}_{\mathrm{Li,an}} - X^{\mathrm{min}}_{\mathrm{Li,an}}}, \qquad [16]$$

where the stoichiometry $\bar{X}_{\mathrm{Li,an}}$ is averaged over the particle diameters (z scale, cf. Fig. 2). The left part of Fig. 8 shows a CC charge at +10 °C. Panel a) shows the metallic lithium volume fraction, and Panel b) shows $\mathrm{SOC_{local}}$ of the anode. As expected, no metallic lithium is formed at +10 °C. We observe that $\mathrm{SOC_{local}}$, which reflects the intercalated lithium stoichiometry, decreases when moving away from the separator, with a 4% difference between the opposite sides of the electrode. This changes when lowering the temperature to −10 °C, as shown in the right part of Fig. 8. From Panel c) we can observe that plating starts at around 660 s, peaking at the end of charge at the maximum value of 3.2 vol.-% at the separator interface where the plated lithium tends to form faster. Panel d) shows $\mathrm{SOC_{local}}$: here plating reaction is competing with intercalation and the SOC reaches a maximum value of only 44%.

Spatiotemporal data for the subsequent CC discharge (without rest and with cut-off at 3.0 V) are shown in Fig. 9. The left panels show results at +10 °C. As no metallic lithium was formed at +10 °C, only the de-intercalation reaction is visible in Fig. 9b. Panels c) and d) show respectively the metallic lithium volume fraction and the $\mathrm{SOC_{local}}$ at −10 °C. It is rather interesting to see in Fig. 9c how the metallic lithium is consumed during the first part of the discharge (2190–2700 s), corresponding to the voltage plateau in Fig. 7a. In Fig. 9d we can actually observe the SOC increasing during this period by nearly 3% due to re-intercalation and then finally decreasing to a minimum value of 13.5% at the end of the CC

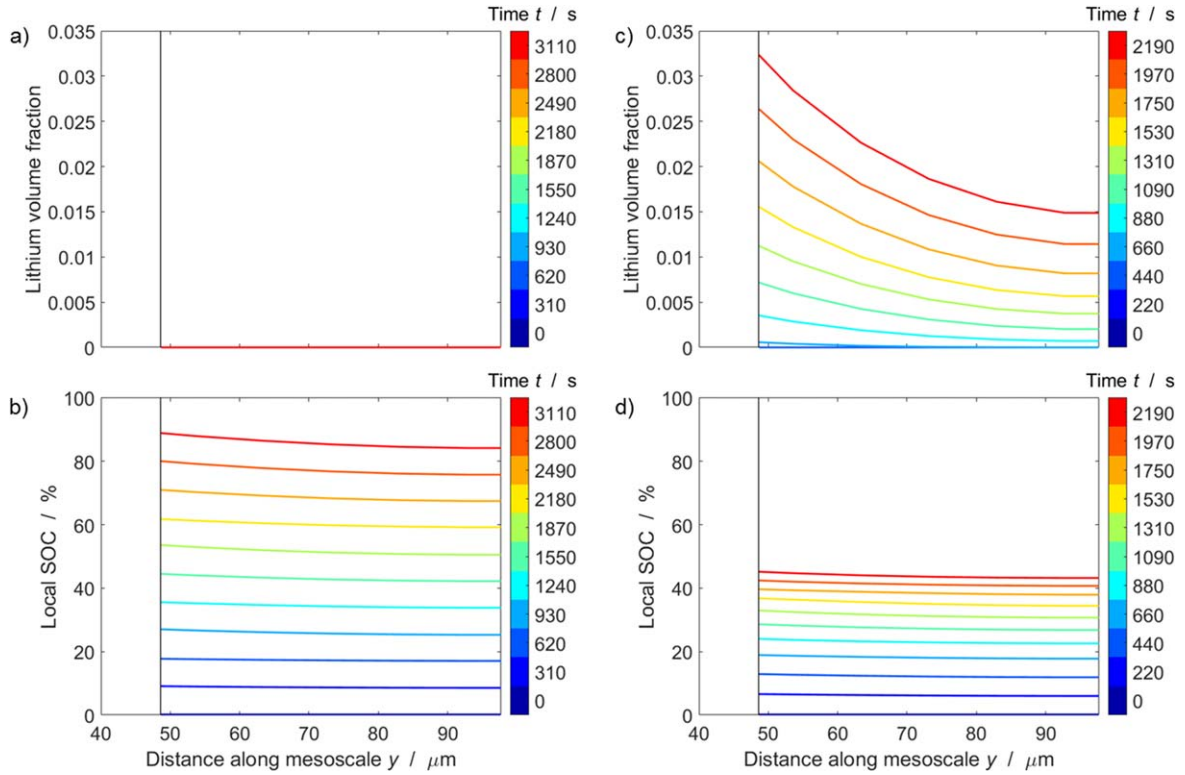

Figure 8. Spatiotemporal behavior along the negative electrode thickness for a 1C CC charge at +10 °C (on the left: (a) lithium volume fraction, (b) local SOC) and −10 °C (on the right: (c) lithium volume fraction, (d) local SOC). The lower end of the mesoscale axis corresponds to the separator, the upper end to the current collector (cf. y scale in Fig. 2).

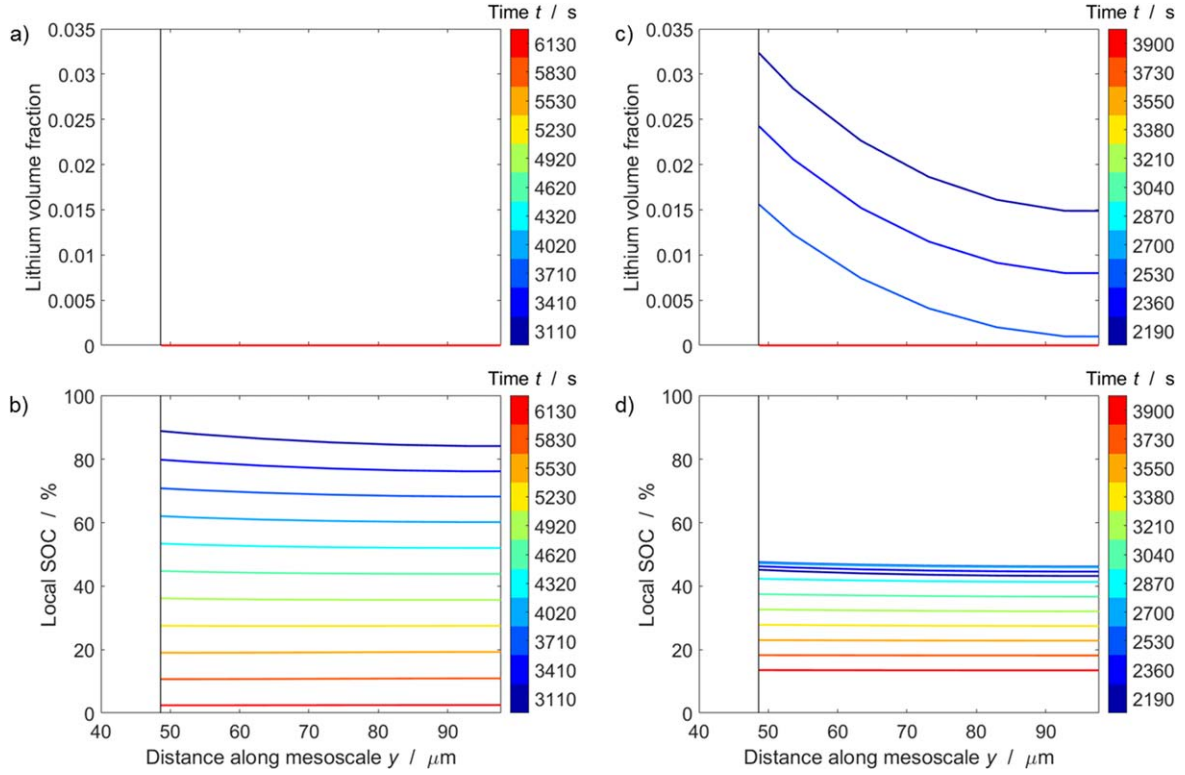

Figure 9. Spatiotemporal behavior along the negative electrode thickness for a 1C CC discharge at +10 °C (on the left: (a) lithium volume fraction, (b) local SOC) and −10 °C (on the right: (c) lithium volume fraction, (d) local SOC). The lower end of the mesoscale axis corresponds to the separator, the upper end to the current collector (cf. y scale in Fig. 2).

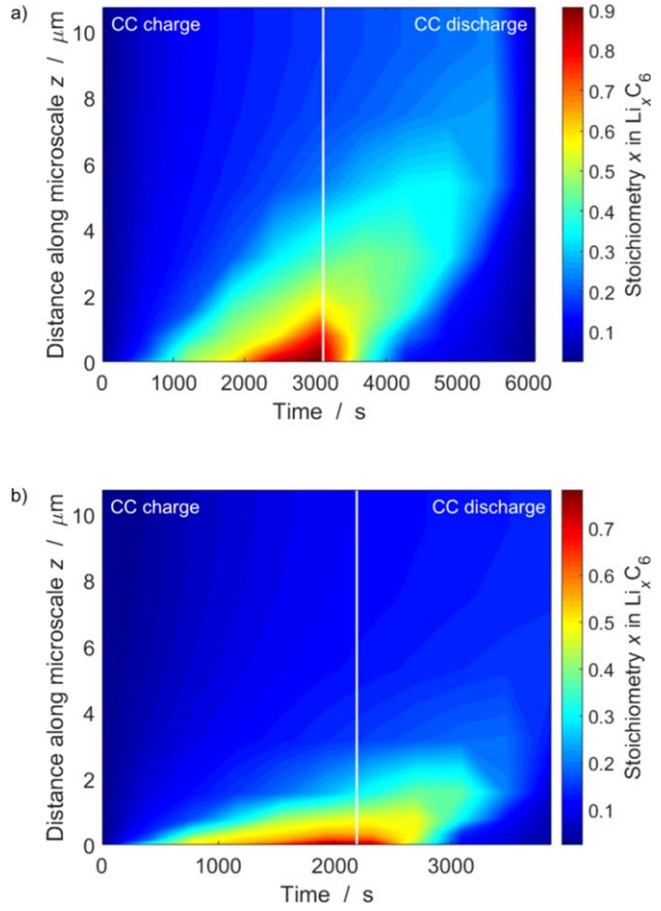

Figure 10. Lithium mole fraction as function of particle diameter (z scale, cf. Fig. 2). Here shown a 1C CC charge-discharge cycle at (a) +10 °C and (b) −10 °C.

discharge, a striking difference with the 2.5% obtained at +10 °C in absence of plating.

We now turn to the microscopic (particle) scale. Figure 10 shows the distribution of lithium stoichiometry inside the graphite particles. These data were taken for a representative particle close to the electrode/separator interface ($y = 48.6$ μm in Fig. 8). The particle surface is at $z = 0$ μm. Figure 10a shows the spatiotemporal behavior for a 1C CC charge-discharge at +10 °C. During the CC charge, we can see the stoichiometry increasing with time and the lithium diffusing along z, with accumulation at the particle surface and values exceeding the nominal stoichiometry upper limit (0.619 at 100% SOC, as shown in our previous work [28]). This means that the graphite particle is locally overcharged (SOC > 100%). During the CC discharge, in the particle bulk the diffusive flux is still directed towards the particle center, while the stoichiometry is rapidly decreasing in the most accessible zones close to the surface. Finally, the de-intercalation is complete at the end of the cycle.

Figure 10b shows the spatiotemporal behavior for a 1C CC charge-discharge at −10 °C. Due to the lower temperature the (thermally-activated) diffusion along z is much slower. The lithium stoichiometry reaches lower values compared to the ones observed in Fig. 10a because the cut-off voltage is reached at an earlier time. The accumulation of lithium close to the particle surface is clearly visible, slightly exceeding the nominal stoichiometry range starting at half way of the CC charge. The surface concentration remains high during the first 500 s of the CC discharge: this is due to re-intercalation of plated lithium. A drop in the stoichiometry around 2600 s indicates full consumption of metallic lithium.

In summary, the intercalation mechanisms at the anode are quite influenced both by the competing plating reaction and by

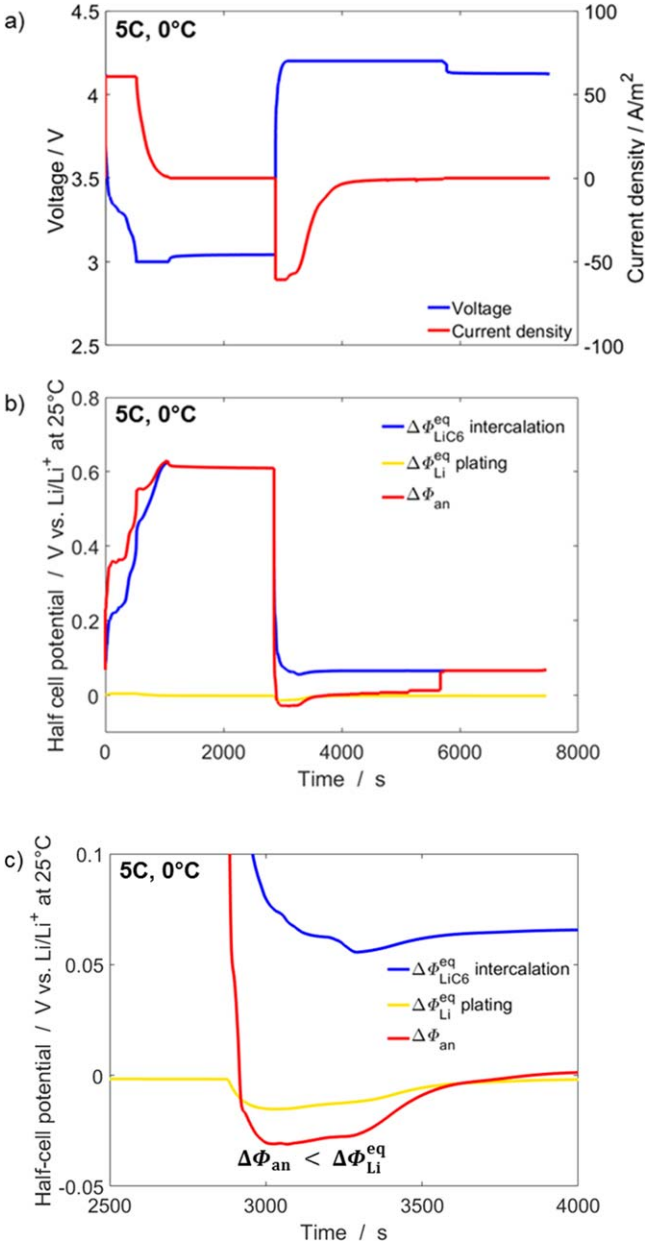

Figure 11. Potential dynamics for a 5C CCCV cycle at 0 °C. Here shown in (a) voltage and current density, (b) equilibrium potentials of the competing reactions (intercalation and plating), together with the anode half-cell potential, (c) zoom in: the plating zone, where $\Delta\Phi_{an} < \Delta\Phi^{eq}_{Li}$ is satisfied.

the low temperatures, such that the concentration profiles differ not only quantitatively, but also qualitatively at different temperatures.

***Plating conditions.*—**In "Thermodynamics and Kinetics of Lithium Plating" we have discussed in detail the thermodynamics and kinetics of lithium plating and pointed out the dominant role of the interplay between plating and intercalation. We now use the mathematical model presented above to investigate this interplay in more detail. To this goal, we have simulated CCCV cycles over a wide range of conditions from 10C down to 0.05C in a temperature range from −20 °C to +30 °C. The used modeling framework includes only the intercalation and plating reactions so it refers to the case of a cell showing evident plating hints. The simulations shown here start at 100% SOC with a constant-current (CC) discharge to

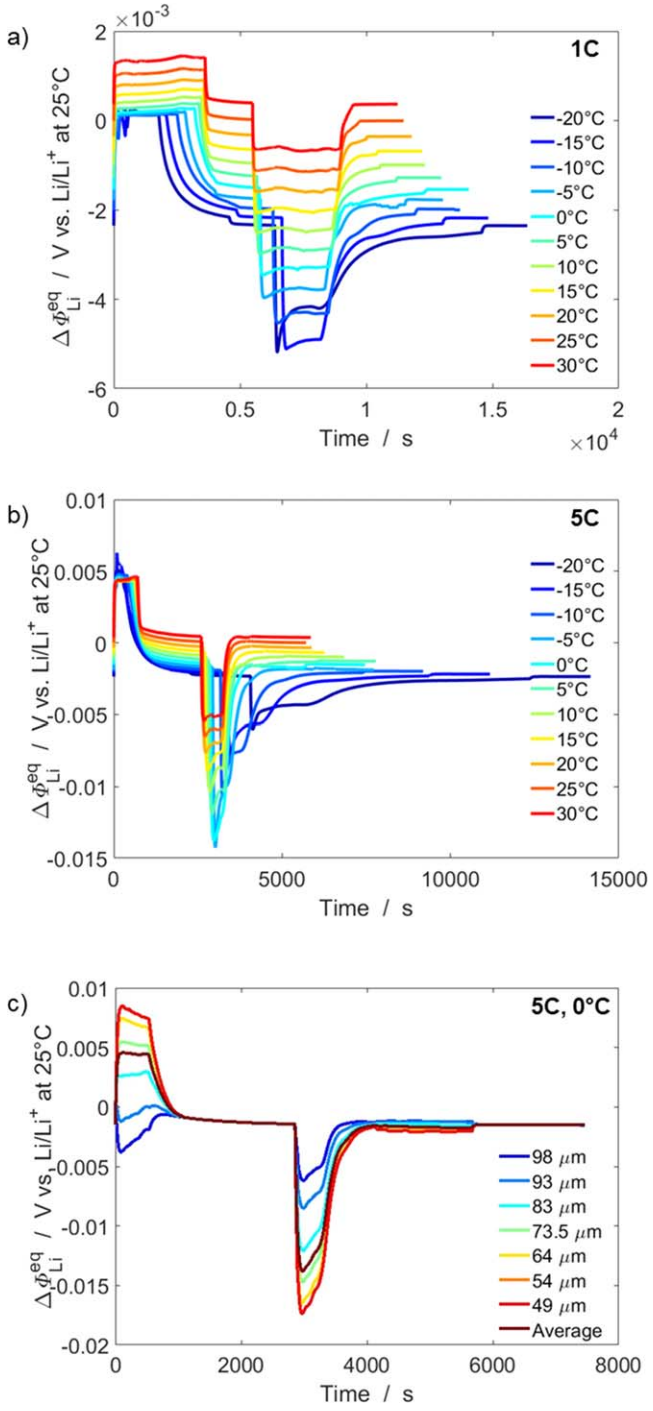

Figure 12. Equilibrium potential of the plating reaction. Here shown (a) 1C at different temperatures, (b) 5C at different temperatures, (c) 5C at 0 °C as function of positions within the anode (49 μm at the separator interface, 98 μm at the current collector interface and "average" as mean value over the total width of the anode).

3.0 V and a constant-voltage (CV) phase with C/20 cut-off current, followed by a 30 min rest and a CCCV charge to 4.2 V with C/20 final current and 30 min rest to reach equilibrium.

Figure 11 gives us an insight into the potential dynamics during a 5C CCCV cycle at 0 °C. Panel a) shows the voltage and the current density. In Fig. 11b the equilibrium potentials $\Delta\Phi^{eq}$ of the two competing reactions (intercalation and plating) are plotted together with the half-cell potential $\Delta\Phi_{an}$ at the anode; Fig. 11c shows a zoom of the same data. As we can see, $\Delta\Phi_{an}$ gets lower than both equilibrium potentials during the CC charge, showing when the plating reaction is favored to intercalation ($\Delta\Phi_{an} < \Delta\Phi_{Li}^{eq}$). From Fig. 11c it can be noted again that in the present model, $\Delta\Phi_{Li}^{eq}$ is not fixed to the canonical value of 0 V vs Li/Li^+, but shows a dynamic variation during cell operation.

Figures 12a and 12b show how $\Delta\Phi_{Li}^{eq}$ changes along the CCCV cycles at different temperatures, respectively for 1C and 5C. Note that the value at 25 °C and a Li^+ concentration of 1 M are the reference conditions for which $\Delta\Phi_{Li}^{eq} = 0$. Consequently, most of the $\Delta\Phi_{Li}^{eq}$ curves will have negative values, especially at low temperatures during charge. Because of the dependence on Li^+ concentration, $\Delta\Phi_{Li}^{eq}$ will also depend on the spatial position within the anode. This is shown in Fig. 12c. It is at the separator interface that we observe a wider range of values for $\Delta\Phi_{Li}^{eq}$, making this interface the most involved zone for plating.

Operation maps.—As plating is known to cause electrode degradation, the insight into its thermodynamics and kinetics obtained at this point can be used for a qualitative assessment of degradation propensity as function of operating conditions. We use the same cycling protocol as described in "Plating conditions". For the results shown in the following, it should be kept in mind that the present model represents a high-power cell; high-energy cells are expected to have an even lower plating threshold.

Tippmann[23] already developed the concept of a degradation factor Θ_I resulting from plating by investigating the thermodynamic plating limit as,

$$\Theta_I = \frac{\int_{\Delta\Phi_{an}<0} I \ dt}{\int I \ dt}. \qquad [17]$$

This expression assumes that plating begins when $\Delta\Phi_{an}$ drops below 0 V. The integrals extend over the charging time only. Here, the capacity (the current integrated) charged under thermodynamic plating condition is normalized to the total capacity during charge. A colormap of Θ_I as function of temperature and charging current is shown in Fig. 13a. According to this map, a harming situation (with highly probable plating formation and consequent electrode degradation) can be found at $T < 0$ °C for most of the C-rates, while "safe" conditions for fast charging are present only when $T > 25$ °C.

Figure 13b shows a colormap where an alternative degradation factor denoted Θ_Φ is plotted over temperature and charging current. Θ_Φ was calculated by using a modified expression according to

$$\Theta_\Phi = \frac{\int_{\Delta\Phi_{an} < \Delta\Phi_{Li}^{eq}} I \ dt}{\int I \ dt}. \qquad [18]$$

Here, the thermodynamic limit for plating is not fixed to 0 V as for Θ_I, but varies along the cycle as predicted by model (cf. "Plating conditions"). Again, the factor is normalized to the total charge to obtain Θ_Φ, and the integrals extend over the charge only. A value of $\Theta_\Phi = 1$ means that the anode potential stays below the plating equilibrium potential $\Delta\Phi_{Li}^{eq}$ during the complete charging process. If plating is absent, as we can see for the warmer temperatures and lower C-rates, the anode potential will always be above this value and $\Theta_\Phi = 0$. According to this map, again a harming situation can be found at most of the conditions when temperatures are under 0 °C, but the "safe" zone appears bigger with "safe" conditions already at 20 °C. Thus, a more accurate representation of the plating thermodynamics is narrowing down the plating region. Both Θ_Φ and Θ_I have maximum values up to around 0.9, meaning that, for the most critical conditions, the largest part of the charging phase is within the thermodynamic plating limit.

These two factors are based on a thermodynamic analysis of plating only. With present model, we have the possibility of assessing also the kinetics. Considering the plating reaction as

parasitic side reaction running in parallel to intercalation, we assess the species formation rates $\dot{s}_{\mathrm{Li}}$ and $\dot{s}_{\mathrm{LiC6}}$ (given in mol $\mathrm{m}^{-3}\,\mathrm{s}^{-1}$), respectively. In particular, we obtain a normalized degradation factor Θ_{Li} by integrating $\dot{s}_{\mathrm{Li}}$ and dividing it by the sum of the integrated $\dot{s}_{\mathrm{LiC6}}$ and $\dot{s}_{\mathrm{Li}}$, both only for positive rates of formation, according to

$$\Theta_{\mathrm{Li}} = \frac{\int_{\dot{s}_{\mathrm{Li}}>0} \dot{s}_{\mathrm{Li}}\,\mathrm{d}t}{\int_{\dot{s}_{\mathrm{LiC6}}>0} \dot{s}_{\mathrm{LiC6}}\,\mathrm{d}t + \int_{\dot{s}_{\mathrm{Li}}>0} \dot{s}_{\mathrm{Li}}\,\mathrm{d}t}. \quad [19]$$

This gives us the ratio of plated lithium to the total amount of lithium involved in the reactions at the anode (intercalated and plated), physically representing a ratio between quantities in $\mathrm{mol}\cdot\mathrm{m}^{-3}$. This degradation factor is therefore more realistic than the thermodynamics-based factors discussed above. The integrals are calculated when the formation rate is positive and not only during the charge process, which allows this degradation factor to include the eventual re-intercalation happening during rest or discharge. Figure 13c shows a colormap where Θ_{Li} is plotted as function of temperature and charging current. The results show a qualitatively similar, but quantitatively different behavior: we see Θ_{Li} peaking at much lower values than before, with a maximum of only 0.3 at low temperatures and high C-rates. Thus, Θ_{Φ} and Θ_{I} strongly overpredict the plating propensity as compared the more realistic Θ_{Li}. Here, "safe" conditions can be found already at 10 °C for most of the currents. This is quite coherent with the simulations and analysis previously shown in this work.

An alternative way of representing degradation at the anode is finally shown in Fig. 13d. As the present model includes a continuity equation for metallic lithium, we can access its volume fraction during cycling. It is likely that large volume fractions cause a high degradation. Therefore, Fig. 13d plots the maximum lithium volume fraction reached during the cycle as function of temperature and C-rate. This colormap shows qualitative differences to the previous ones, in particular, the highest values of plated lithium occur not at the lowest T, but in the temperature zone between −10 and 0 °C. Both plating and intercalation reactions are slowed down at these temperatures, but the interplay between the two finds plating in a more competitive position, due to its smaller activation energy, and at the same time the solid-state transport is not as heavily affected as at the lowest temperatures. We clearly see here plating to be caused by a combination of thermodynamics, kinetics and transport working and counteracting in different ways.

Figure 14 shows a comparison of the approaches at 5C. Here the values from the four degradation factors, normalized to their individual maximum value reached over the full colormap range, are plotted vs temperature to highlight the similarities and differences between them. A "safe" zone is present above 20 °C for all the

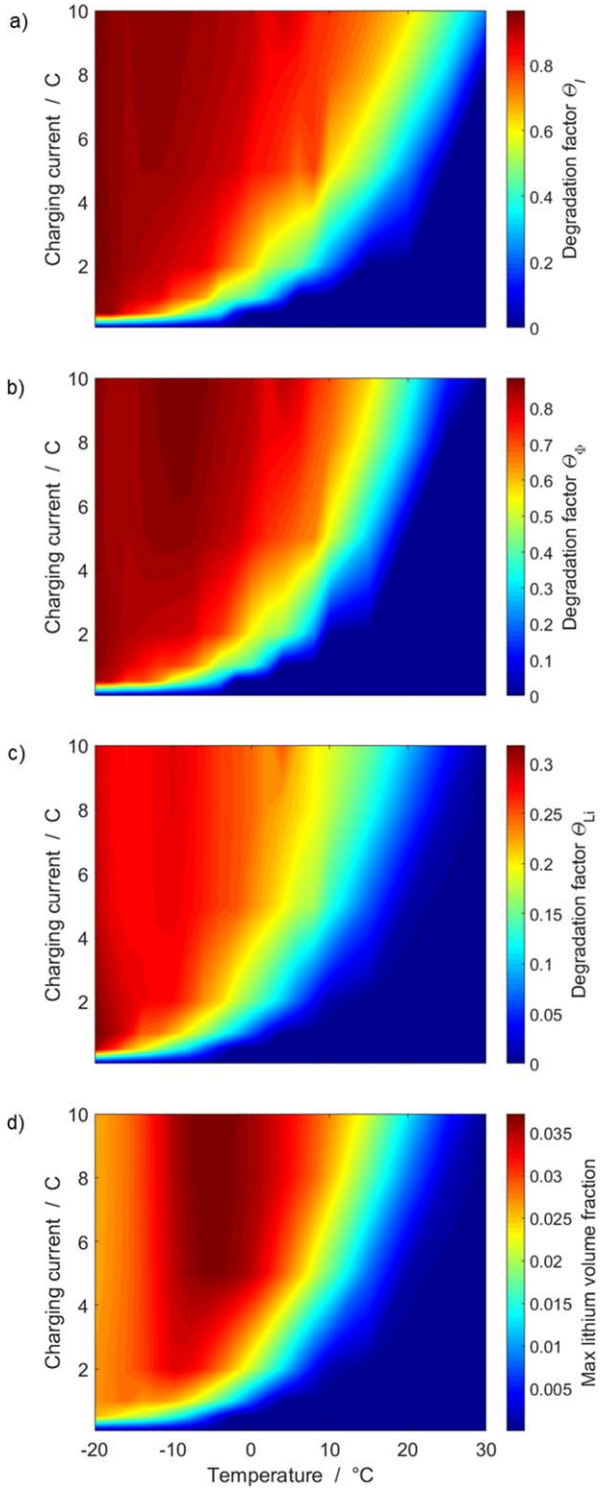

Figure 13. Operation colormaps of a CCCV cycle. In (a) the Θ_I degradation factor represents the ratio of charge input when the potential condition for plating $\Delta\Phi_{\mathrm{an}} < 0$ is satisfied (0 = never, 1 = always). In (b) the Θ_{Φ} degradation factor is based on the potential condition for plating $\Delta\Phi_{\mathrm{an}} < \Delta\Phi_{\mathrm{Li}}^{\mathrm{eq}}$. In (c) the Θ_{Li} degradation factor is defined as ratio of the integrated plating rate over the integrated total reaction rate. In (d) the peak value of plated lithium volume fraction formed during cycling is used as degradation indicator, where a value of zero means no metallic lithium was formed.

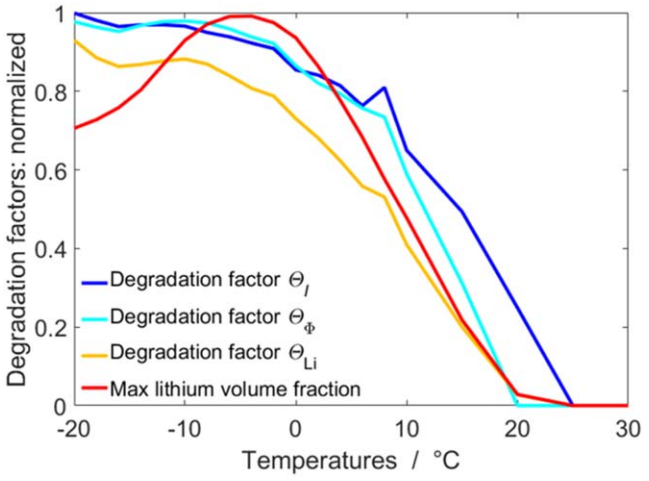

Figure 14. Degradation factors from the colormaps in Fig. 13, normalized to their respective maximum values. Here are shown the curves for 5C. The plot highlights the differences between the four different methods and helps in their comparison.

degradation factors except Θ_I that tends to be most pessimistic. For temperatures under 0 °C, Θ_I and Θ_Φ behave quite similar, while Θ_{Li} shows always lower values, with all the three having their peak at the lowest temperature. Finally the fourth curve, representing the plated lithium volume fraction, has instead a different behavior with the most harming values in the zone between −10 °C and 0 °C, as described above.

The presented colormaps are useful tools, as they enable a fast overview on the operational harming conditions in terms of lithium plating based on the complex multi-scale multi-physical model.

Summary and Conclusions

We have presented the extension of a previously-developed P3D model of a commercial 350 mAh high-power lithium-ion pouch cell with the purpose of simulating reversible lithium plating over a wide range of conditions. A systematic approach towards parameterization of the plating reaction was used, using an extensive literature research to choose a coherent set of thermodynamic and kinetic parameters. The model optionally includes a re-intercalation reaction that was shown to suppress macroscopic plating hints. Validation of the model with and without this extra reaction was possible by comparison respectively with experiments on our reference cell and published experimental data in which the most common plating features (*voltage plateau* and *voltage drop*) are present. These features were reproduced qualitatively in the simulations for both cases. However, the simulations still showed quantitative differences to the experimental data. These differences may be related to morphological features of the plated lithium, which are not included in the present model, but which are likely to affect the ratio of solution-mediated vs surface-mediated re-intercalation.

The model allows an in-depth spatiotemporal analysis of the anode behavior at the mesoscopic and microscopic scales, demonstrating the dynamic and nonlinear interaction between the intercalation and plating reactions. It is worth noting that in our model the equilibrium potential of the plating reaction is not always equal to 0 V, as often assumed in literature, but varies according to the local temperature and lithium-ion concentration. Finally, different definitions of "degradation factors" were presented. Operational maps were shown and discussed as a practical and intuitive way to assess reversible plating propensity during CCCV cycles over a wide range of conditions.

The present model is limited to reversible plating, that is, plated lithium was allowed to either re-intercalate or being electrochemically oxidized. Irreversible lithium plating, characterized by the breaking of dendrites and the formation and isolation of dead lithium[8,63–65] from the graphite, is not considered here; neither is the formation a solid electrolyte interface (SEI) on the plated lithium. Both effects will be subject of future studies with the goal of quantitatively predicting capacity loss of lithium-ion batteries resulting from plating.

Acknowledgments

This work was funded by the Deutsche Forschungsgemeinschaft (German Research Foundation, DFG) in the framework of the research training group SiMET—Simulation of Mechanical, Electrical and Thermal Effects in Li-ion Batteries (281041241/GRK 2218). The authors thank Mehmet Yagci (Hochschule Offenburg) for supporting the experimental measurements.

Appendix

Model equations.—The following Table summarizes the model equations. The reader is referred to Ref. 43 for a detailed model description including the derivation of the equations. Tables including all model parameters, species properties and the rate coefficients for the chemical reactions (except the plating reaction) can be found in our previous work.[28] A list of symbols is given in Appendix.

Macroscale (*x* direction): Heat transport in cell

Energy conservation

$$\rho c_p \frac{\partial T}{\partial t} = \frac{\partial}{\partial x}\left(\lambda \frac{\partial T}{\partial x}\right) + \dot{q}^V$$

Heat flux at cell surface

$$J_q = \alpha(T - T_{amb}) + \epsilon\sigma_{SB}(T^4 - T_{amb}^4)$$

Total heat sources

$$\dot{q}^V = \frac{A_e}{V_{cell}}\left(\int_0^{L_{EP}} (\dot{q}_{chem}(y) + \dot{q}_{ohm}(y))dy + R_{cc} i^2\right)$$

Chemistry heat source

$$\dot{q}_{chem} = \sum_{n=1}^{N_r} (r_n A_n^V (-\Delta H_n + F\nu_{e,n}\Delta\Phi_n))$$

Ohmic heating

$$\dot{q}_{ohm} = \sigma_{elyt} \cdot \left(\frac{\partial \Phi_{elyt}}{\partial y}\right)^2$$

Mesoscale (*y* direction): Mass and charge transport in electrode pair

Mass conservation of species i

$$\frac{\partial(\varepsilon_{elyt} c_i)}{\partial t} = -\frac{\partial J_i}{\partial y} + \dot{s}_i^V + \dot{s}_{i,DL}^V$$

Charge conservation

$$C_{DL}^V \frac{\partial(\Delta\Phi)}{\partial t} = \sum_i Z_i F \frac{\partial J_i}{\partial y} - i_F^V$$

Species fluxes: Nernst-Planck

$$J_i = -D_i^{eff} \frac{\partial c_i}{\partial y} - \frac{z_i F}{RT} c_i D_i^{eff} \frac{\partial \Phi_{elyt}}{\partial y}$$

Microscale (*z* direction): Mass transport in active materials particle

Mass conservation (Fick's 2nd law)

$$\frac{\partial c_{Li,AM}}{\partial t} = \frac{1}{z^2}\frac{\partial}{\partial z}\left(z^2 D_{Li,AM} \frac{\partial c_{Li,AM}}{\partial z}\right)$$

Electrochemistry[a)]

Interfacial rate of reaction n

$$r_n = \frac{i_n}{F} = \frac{{i_n}^0}{F}\left[\exp\left(\frac{\alpha_c z F}{RT}\eta_{act,n}\right) - \exp\left(-\frac{(1-\alpha_c) z F}{RT}\eta_{act,n}\right)\right]$$

Overpotential

$$\eta_{act,n} = \Delta\Phi^{eff} - \Delta\Phi_n^{eq} = \Delta\Phi - R_{SEI}^V i_F^V - \Delta\Phi_n^{eq}$$

Species source terms

$$\dot{s}_i^V = \sum_{n=1}^{N_r} (\nu_i r_n A_n^V)$$

(Continued).

Current, voltage, potentials	
Cell voltage	$E = \Phi_{\text{elde,ca}} - \Phi_{\text{elde,an}} - i \cdot R_{\text{cc}}$
Cell current	$I_{\text{cell}} = \frac{A_{\text{e}}}{V_{\text{cell}}} \cdot \int_{y=0}^{L_{\text{electrode}}} (i_{\text{F}}^{V} + i_{\text{DL}}^{V})\text{d}y$
Faradaic current density	$i_{\text{F}}^{V} = F\dot{s}_{\text{e}}^{V} = \sum_{n=1}^{N_{\text{r}}} F(\nu_{\text{e},n} r_n A_n^{V})$
Double layer current density	$i_{\text{DL}}^{\text{V}} = C_{\text{DL}}^{\text{V}} \frac{\text{d}(\Delta\Phi)}{\text{d}t}$
Source term from double layer	$\dot{s}_{i,\text{DL}}^{\text{V}} = \frac{z_i}{F} i_{\text{DL}}^{\text{V}}$ with $i = \text{Li}^+$
Potential step (anode and cathode)	$\Delta\Phi = \Phi_{\text{elde}} - \Phi_{\text{elyt}}$
Multi-phase management	
Volume fraction of phases	$\frac{\partial(\rho_j \varepsilon_j)}{\partial t} = \sum_{i=1}^{N_{\text{R},j}, N_{\text{P},j}} \dot{s}_i^{\text{V}} M_i$
Feedback on transport coefficients (porous electrode theory)	$D_i^{\text{eff}} = \frac{\varepsilon_{\text{elyt}}}{\tau_{\text{elyt}}{}^2} D_i$

a) as implemented in Cantera.

List of symbols

Symbol	Unit	Meaning
A_{e}	m^2	Active electrode area
A_n^{V}	$\text{m}^2\cdot\text{m}^{-3}$	Volume-specific surface area of reaction n
a_{n} b_{n}	1	NASA polynomial coefficients
α_{sn}	m^{-1}	Specific surface area
C_{DL}^{V}	$\text{F}\cdot\text{m}^{-3}$	Volume-specific double-layer capacity
c_i	$\text{mol}\cdot\text{m}^{-3}$	Concentration of species i in a bulk phase
c_i^0	$\text{mol}\cdot\text{m}^{-3}$	Standard concentration of species i
$c_{\text{Li}^+[\text{elyt}]}$	$\text{mol}\cdot\text{m}^{-3}$	Concentration of solved Li-ions
c_{Li}	$\text{mol}\cdot\text{m}^{-3}$	Concentration of lithium in the active material
$c_{\text{Li}}^{\text{max}}$	$\text{mol}\cdot\text{m}^{-3}$	Maximum amount of lithium stored in the active material
$c_{p,i}^0$	$\text{J}\cdot\text{mol}^{-1}\ \text{K}^{-1}$	Molar heat capacity of species i
c_{P}	$\text{J}\cdot\text{kg}^{-1}\cdot\text{K}^{-1}$	Specific heat capacity
D_i	$\text{m}^2\cdot\text{s}^{-1}$	Diffusion coefficient of species i
D_i^{eff}	$\text{m}^2\cdot\text{s}^{-1}$	Effective diffusion coefficient of species i
E_{exp}, E_{OC}	V	Experimental and open circuit voltage
E_{act}	$\text{J}\cdot\text{mol}^{-1}$	Activation energy of forward reaction
F	$\text{C}\cdot\text{mol}^{-1}$	Faraday's constant
ΔG^0	$\text{J}\cdot\text{mol}^{-1}$	Standard Gibbs free reaction energy
ΔH_n	$\text{J}\cdot\text{mol}^{-1}$	Reaction enthalpy of reaction n
h_i^0	$\text{kJ}\cdot\text{mol}^{-1}$	Molar enthalpy of species i
i	1	Index of species
i	$\text{A}\cdot\text{m}^{-2}$	Area-specific current (with respect to A_{e})
i^0	$\text{A}\cdot\text{m}^{-2}$	Exchange current density
i^{00}	$\text{A}\cdot\text{m}^{-2}$	Exchange current density factor
$i_{\text{lim ,c}}$	$\text{A}\cdot\text{m}^{-2}$	Cathodic limiting current
i_F^{V}	$\text{A}\cdot\text{m}^{-3}$	Volume-specific faradaic current
j	1	Index of bulk phases
J_{q}	$\text{W}\cdot\text{m}^{-2}$	Heat flux from cell surface
J_{i}	$\text{mol}\cdot\text{m}^{-2}\cdot\text{s}^{-1}$	Molar flux of species i
$j_{\text{V,Li}}$	$\text{A}\cdot\text{m}^{-3}$	Volumetric current density (plating reaction)
j_{tot}	$\text{A}\cdot\text{m}^{-3}$	Volumetric current density (total)
k	mol, m, s ([a])	Reaction rate constant
$L_{\text{electrode}}$	m	Thickness of electrode
L_{EP}	m	Thickness of electrode pair
M_i	$\text{kg}\cdot\text{mol}^{-1}$	Molar mass of species i
N_{P}	1	Number of products participating in reaction
N_{R}	1	Number of reactants participating in reaction
N_{r}	1	Number of reactions
p	$\text{kg}\cdot\text{m}^{-1}\cdot\text{s}^{-2}$	Pressure
$\dot{q}_{\text{chem}}$	$\text{W}\cdot\text{m}^{-2}$	Heat source due to chemical reactions

(Continued).

$\dot{q}_{\text{ohm}}$	$\text{W}\cdot\text{m}^{-2}$	Heat source due to ohmic losses
$\dot{q}^{\text{V}}$	$\text{W}\cdot\text{m}^{-3}$	Volume-specific heat source
R	$\text{J}\cdot\text{K}^{-1}\cdot\text{mol}^{-1}$	Ideal gas constant
R_{cc}	$\Omega\cdot\text{m}^2$	Area-specific ohmic resistance of current collection system
R_{ct}	$\Omega\cdot\text{m}^2$	Area-specific charge transfer resistance
R	Ω	Total internal resistance
R_{film}	$\Omega\cdot\text{m}^2$	Area-specific ohmic resistance of the surface film
$R^{\text{V}}_{\text{SEI}}$	$\Omega\cdot\text{m}^3$	Volume-specific ohmic resistance of SEI film
r_n	$\text{mol}\cdot\text{m}^{-2}\cdot\text{s}^{-1}$	Interfacial reaction rate of reaction n
$\dot{s}_i$	$\text{mol}\cdot\text{m}^{-3}\cdot\text{s}^{-1}$	Formation rate of species i
s^0_i	$\text{J}\cdot\text{mol}^{-1}\cdot\text{K}^{-1}$	Molar entropy of species i
$\dot{s}^{\text{V}}_i$	$\text{mol}\cdot\text{m}^{-3}\cdot\text{s}^{-1}$	Volumetric species source term
$\dot{s}^{\text{V}}_{\text{i,DL}}$	$\text{mol}\cdot\text{m}^{-3}\cdot\text{s}^{-1}$	Volumetric species source term due to double layer charge/discharge
t	s	Time
T	K	Temperature
T^0	K	Standard temperature 298.15 K
T_{amb}	K	Ambient temperature (cell surrounding)
V_{cell}	m^3	Volume of cell
x	m	Spatial position in dimension of battery thickness
X_{Li}	1	Stoichiometry of lithium in the active material
SOC	1	State-Of-Charge
y	m	Spatial position in dimension of electrode-pair thickness
z	m	Spatial position in dimension of particle thickness
z	1	Number of electrons transferred in charge-transfer reaction
α	$\text{W}\cdot\text{m}^{-2}\cdot\text{K}^{-1}$	Heat transfer coefficient
α_{a}, α_{c}	1	Anodic and cathodic transfer coefficients of electrochemical reaction
Φ_{s}, Φ_{elyt}	V	Electric potential in the solid phase and in the electrolyte
$\Delta\Phi^{\text{eq}}$	V	Equilibrium potential difference
$\Delta\Phi_{\text{an}}$	V	Electric potential of the anode electrode
$\Delta\Phi^{\text{eq}}_{\text{Li}}$	V	Equilibrium potential of plating reaction
$\Delta\Phi_{\text{n}}$	V	Electric potential difference of reaction n
ϵ	1	Emissivity of the cell surface
$\varepsilon_{\text{elyt}}$	1	Volume fraction of the electrolyte
ε_j	1	Volume fraction of bulk phase j
η_{act}	V	Activation overpotential
λ	$\text{W}\cdot\text{m}^{-1}\cdot\text{K}^{-1}$	Thermal conductivity
μ^0_i	$\text{J}\cdot\text{mol}^{-1}$	Standard-state chemical potentials of all species i
ν_i	1	Stoichiometric coefficient of species i
$\nu_{\text{e},n}$	1	Stoichiometric coefficient of electrochemical reaction n
ρ	$\text{kg}\cdot\text{m}^{-3}$	Density
σ	$\text{S}\cdot\text{m}^{-1}$	Electrolyte conductivity
σ_{SB}	$\text{W}\cdot\text{m}^{-2}\cdot\text{K}^{-4}$	Stefan-Boltzmann constant
τ_{elyt}	1	Geometric tortuosity of the electrolyte
Θ_I	1	Simulated degradation factor ($\Delta\Phi_{\text{an}} < 0$)
Θ_Φ	1	Simulated degradation factor ($\Delta\Phi_{\text{an}} < \Delta\Phi^{\text{eq}}_{\text{Li}}$)
Θ_{Li}	1	Simulated degradation factor ($\dot{s}_{\text{Li}} > 0$)

a) Units of mol, m and s depending on reaction stoichiometry.

ORCID

Serena Carelli https://orcid.org/0000-0001-8959-6813
Wolfgang G. Bessler https://orcid.org/0000-0001-8037-9046

References

1. I. D. Campbell, M. Marzook, M. Marinescu, and G. J. Offer, *J. Electrochem. Soc.*, **166**, A725 (2019).
2. J. M. Reniers, G. Mulder, and D. A. Howey, *J. Electrochem. Soc.*, **166**, A3189 (2019).
3. S. J. Harris, A. Timmons, D. R. Baker, and C. Monroe, *Chem. Phys. Lett.*, **485**, 265 (2010).
4. J. Remmlinger, S. Tippmann, M. Buchholz, and K. Dietmayer, *J. Power Sources*, **254**, 268 (2014).
5. B. V. Ratnakumar and M. C. Smart, *ECS Trans.*, **25**, 241 (2010).
6. M. C. Smart and B. V. Ratnakumar, *J. Electrochem. Soc.*, **158**, A379 (2011).
7. M. C. Smart, B. V. Ratnakumar, L. Whitcanack, K. Chin, M. Rodriguez, and S. Surampudi, *IEEE Aerosp. Electron. Syst. Mag.*, **17**, 16 (2002).
8. M. Petzl and M. A. Danzer, *J. Power Sources*, **254**, 80 (2014).
9. M. Petzl, M. Kasper, and M. A. Danzer, *J. Power Sources*, **275**, 799 (2015).
10. V. Zinth, C. von Lüders, M. Hofmann, J. Hattendorff, I. Buchberger, S. Erhard, J. Rebelo-Kornmeier, A. Jossen, and R. Gilles, *J. Power Sources*, **271**, 152 (2014).
11. W. Lu, C. M. López, N. Liu, J. T. Vaughey, A. Jansen, and D. Dennis W., *J. Electrochem. Soc.*, **159**, A566 (2012).
12. C. Uhlmann, J. Illig, M. Ender, R. Schuster, and E. Ivers-Tiffée, *J. Power Sources*, **279**, 428 (2015).
13. C. von Lüders, V. Zinth, S. V. Erhard, P. J. Osswald, M. Hofmann, R. Gilles, and A. Jossen, *J. Power Sources*, **342**, 17 (2017).
14. M. Ecker, "Lithium plating in lithium-ion batteries: an experimental and simulation approach." *PhD Thesis*, RWTH Aachen University (2016).
15. A. H. Whitehead, *J. Electrochem. Soc.*, **144**, L92 (1997).
16. J. Fan and S. Tan, *Electrochim. Acta*, **153**, A1081 (2006).
17. H.-P. Lin, D. Chua, M. Salomon, H.-C. Shiao, M. Hendrickson, E. Plichta, and S. Slane, *J. Electrochem. Soc.*, **4**, A71 (2001).

18. S. Schindler, M. Bauer, M. Petzl, and M. A. Danzer, *J. Power Sources*, **304**, 170 (2016).
19. T. R. Tanim, E. J. Dufek, C. C. Dickerson, and S. M. Wood, *J. Electrochem. Soc.*, **166**, A2689 (2019).
20. A. A. Franco, M. L. Doublet, and W. G. Bessler (ed.), *Physical Multiscale Modeling and Numerical Simulation of Electrochemical Devices for Energy Conversion and Storage: From Theory to Engineering to Practice* (Springer, London, Heidelberg, New York, Dordrecht) (2016).
21. R. D. Perkins, A. V. Randall, X. Zhang, and G. L. Plett, *J. Power Sources*, **209**, 318 (2012).
22. S. Tippmann, "Modellierung und experimentelle Charakterisierung des Degradationsverhaltens durch Lithium-Plating an Lithium-Ionen-Zellen unter automobilen Betriebsbedingungen." *PhD Thesis*, Stuttgart University (2016).
23. S. Tippmann, D. Walper, L. Balboa, B. Spier, and W. G. Bessler, *J. Power Sources*, **252**, 305 (2014).
24. T. Danner, M. Singh, S. Hein, J. Kaiser, H. Hahn, and A. Latz, *J. Power Sources*, **334**, 191 (2016).
25. S. Hein and A. Latz, *Electrochim. Acta*, **201**, 354 (2016).
26. X.-G. Yang, S. Ge, T. Liu, Y. Leng, and C.-Y. Wang, *J. Power Sources*, **395**, 251 (2018).
27. X.-G. Yang, Y. Leng, G. Zhang, S. Ge, and C.-Y. Wang, *J. Power Sources*, **360**, 28 (2017).
28. S. Carelli, M. Quarti, M. C. Yagci, and W. G. Bessler, *J. Electrochem. Soc.*, **166**, A2990 (2019).
29. P. W. Atkins, *Physical chemistry* (Oxford University Press, Oxford, UK) (1998).
30. Z. Li, J. Huang, B. Yann Liaw, V. Metzler, and J. Zhang, *J. Power Sources*, **254**, 168 (2014).
31. Q. Liu, C. Du, B. Shen, P. Zuo, X. Cheng, Y. Ma, G. Yin, and Y. Gao, *RSC Adv.*, **6**, 88683 (2016).
32. T. Waldmann, B.-I. Hogg, and M. Wohlfahrt-Mehrens, *J. Power Sources*, **384**, 107 (2018).
33. J. Newman and K. E. Thomas-Alyea, *Electrochemical Systems* (John Wiley & Sons, Hoboken, New Jersey, USA) (2004).
34. B. J. McBride, M. J. Zehe, and S. Gordon, *NASA Glenn Coefficients for Calculating Thermodynamic Properties of Individual Species* (NASA, Ohio, USA) (2002).
35. B. J. McBride, S. Gordon, and M. A. Reno, *Coefficients for Calculating Thermodynamic and Transport Properties of Individual Species* (NASA, Ohio, USA) (1993).
36. M. J. Lampinen, *J. Electrochem. Soc.*, **140**, 3537 (1993).
37. R. Bhattacharyya and S. C. Lahiri, *Z. Phys. Chem.*, **231**, 304 (2017).
38. D. D. Wagman, *The NBS tables of chemical thermodynamic properties: Selected values for inorganic and C1 and C2 organic substances in SI units* (American Chemical Soc., New York, NY) (1982).
39. Y. Yamada and A. Yamada, *J. Electrochem. Soc.*, **162**, A2406 (2015).
40. M. Mayur, S. C. DeCaluwe, B. L. Kee, and W. G. Bessler, *Electrochim. Acta*, **323**, 134797 (2019).
41. M. Mayur, M. C. Yagci, S. Carelli, P. Margulies, D. Velten, and W. G. Bessler, *Physical chemistry chemical physics: PCCP*, **21**, 23672 (2019).
42. H. Moon, R. Tatara, T. Mandai, K. Ueno, K. Yoshida, N. Tachikawa, T. Yasuda, K. Dokko, and M. Watanabe, *J. Phys. Chem. C*, **118**, 20246 (2014).
43. C. Kupper and W. G. Bessler, *J. Electrochem. Soc.*, **164**, A304 (2017).
44. M. W. Verbrugge and B. J. Koch, *J. Electroanal. Chem.*, **367**, 123 (1994).
45. G. Bieker, M. Winter, and P. Bieker, *Physical chemistry chemical physics: PCCP*, **17**, 8670 (2015).
46. R. Tao, X. Bi, S. Li, Y. Yao, F. Wu, Q. Wang, C. Zhang, and J. Lu, *ACS applied materials & interfaces*, **9**, 7003 (2017).
47. S. G. Meibuhr, *J. Electrochem. Soc.*, **117**, 56 (1970).
48. S.-I. Lee, U.-H. Jung, Y.-S. Kim, M.-H. Kim, D.-J. Ahn, and H.-S. Chun, *Korean J. Chem. Eng.*, **19**, 638 (2002).
49. P. Arora, *J. Electrochem. Soc.*, **146**, 3543 (1999).
50. R. Jasinski, *Advances in Electrochemistry and Electrochemical Engineering*, ed. P. Delahay and C. W. Tobias (Wiley-Interscience, New York) (1971).
51. H. Ge, T. Aoki, N. Ikeda, S. Suga, T. Isobe, Z. Li, Y. Tabuchi, and J. Zhang, *J. Electrochem. Soc.*, **164**, A1050 (2017).
52. S. Lueth, "Untersuchung des Einflusses der Mikrostruktur von Kathoden auf das Entladeverhalten von Lithiumionenhalbzellen." *PhD Thesis*, Stuttgart University (2015).
53. R. Chandrasekaran and T. F. Fuller, *J. Electrochem. Soc.*, **158**, A859 (2011).
54. M. Doyle, *J. Electrochem. Soc.*, **140**, 1526 (1993).
55. T. F. Fuller, *J. Electrochem. Soc.*, **141**, 1 (1994).
56. M. Doyle, *J. Electrochem. Soc.*, **143**, 1890 (1996).
57. T. R. Jow, M. B. Marx, and J. L. Allen, *J. Electrochem. Soc.*, **159**, A604 (2012).
58. C. Sequeira and A. Hooper, *Solid State Ionics*, **9–10**, 1131 (1983).
59. R. Ehrig, U. Nowak, L. Oeverdieck, and P. Deuflhard, in*High performance scientific and engineering computing. Lecture notes in computational science and engineering*, ed. H.-J. Bungartz, F. Durst, and C. Zenger (Springer, Berlin) p. 233 (1999).
60. P. Deuflhard, E. Hairer, and J. Zugck, *Numer. Math.*, **51**, 501 (1987).
61. D. G. Goodwin, R. L. Speth, H. K. Moffat, and B. W. Weber, *Cantera: An Object-oriented Software Toolkit For Chemical Kinetics, Thermodynamics, And Transport Processes* (2019), DOI:https://doi.org/10.5281/zenodo.1174508.
62. N. N. Greenwood and A. Earnshaw, *Chemie der Elemente* (VCH, Weinheim) (1990).
63. J. Steiger, D. Kramer, and R. Mönig, *Electrochim. Acta*, **136**, 529 (2014).
64. K.-H. Chen, K. N. Wood, E. Kazyak, W. S. LePage, A. L. Davis, A. J. Sanchez, and N. P. Dasgupta, *J. Mater. Chem. A*, **5**, 11671 (2017).
65. I. Yoshimatsu, *J. Electrochem. Soc.*, **135**, 2422 (1988).